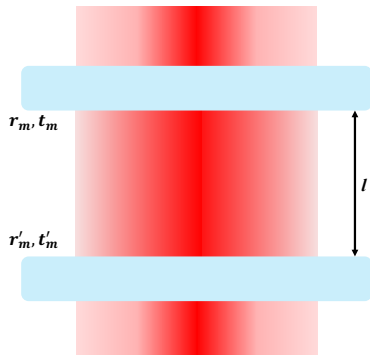


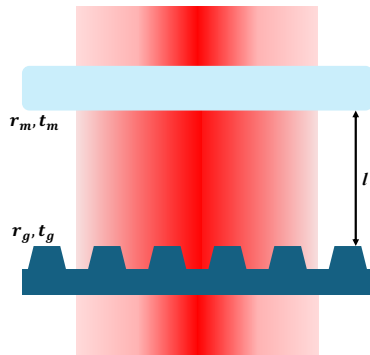
Contents

1	Introduction	1
2	Theory	2
2.1	The Fabry-Perot interferometer	2
2.1.1	Transmission	2
2.1.2	Varying the cavity length	4
2.1.3	Varying the incident wavelength	6
2.1.4	Cavity losses	7
2.2	The Fano mirror: a sub wavelength grating	9
2.2.1	Reflection/transmission spectra and line shape analysis	9
2.2.2	Lossless grating	9
2.2.3	Lossy grating	13
2.3	The single Fano cavity	14
2.3.1	The single Fano cavity model	14
2.3.2	Transmission linewidth	15
2.4	The double Fano cavity	19
2.4.1	The double Fano cavity model	19
2.4.2	Transmission linewidth	20
2.4.3	Single and double Fano cavity comparison	21
2.4.4	Additional cavity losses	24
2.4.5	Spectral detuning (lossless)	25
2.4.6	Spacial detuning (lossless)	28
3	Method	35
3.1	The experimental setup	35
3.1.1	Tunable diode laser	36
3.1.2	$\lambda/2$ - waveplate	37
3.1.3	Optical telescope	38
3.1.4	Transmission, reflection and incident photo-detectors	38
3.1.5	The double Fano cavity measurement setup	39
3.1.6	Acoustic noise reduction	42
3.1.7	Additional equipment used	42
3.2	Characterization of sub-wavelength grating	43
3.2.1	The alignment procedure	43
3.2.2	Adjusting and measuring the beam waist	46
3.2.3	Obtaining normalized transmission/reflection spectra	48

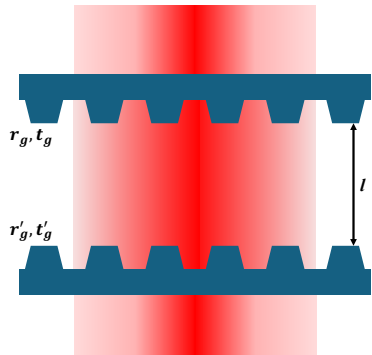
3.3	Cavity measurements	49
3.3.1	Aligning the double Fano cavity	50
3.3.2	Cavity resonance - the piezo ring	52
3.3.3	Determining the cavity length	55
3.3.4	Recording normalized spectra	55
3.3.5	Centering of the top grating	57
3.3.6	Estimating parallelism	60
4	Simulations	62
4.1	The single Fano cavity	62
4.2	The double Fano cavity	62
5	Experimental results	63
5.1	The single Fano cavity	63
5.2	The double Fano cavity	63
5.2.1	Realizing the double fano model	63
5.2.2	Double fano off-resonance Fabry-Perot cavity	64
5.2.3	The double fano linewidth	64
6	Discussion	65
6.1	Optimal configuration for double fano cavity - spacial limitation for the cavity length	65
6.2	Spacial drift of the piezo ring	65
6.3	Noise reduction - coupled/uncoupled mechanical/acoustic vibra- tion (the plexi-glass box)	65
6.4	Broadening sources (especially for long cavities)	65
6.5	Improvements to the setup	65
7	Appendix	66
7.1	Simulated broadband and single Fano cavity resonance transmis- sion spectra	66
7.2	Simulated single and double Fano cavity resonance intracavity spectra	68
8	References	70



(a) Broadband cavity.



(b) Single Fano cavity.



(c) Double Fano cavity.

1 Introduction

2 Theory

2.1 The Fabry-Perot interferometer

The Fabry-Perot interferometer, also known as an optical cavity, is generally comprised of two reflective optical elements, hereafter referred to as mirrors. In the following we assume a plane-plane configuration for two lossless mirrors and a plane-wave at normal incidence for the incoming field, as sketched in figure 2.

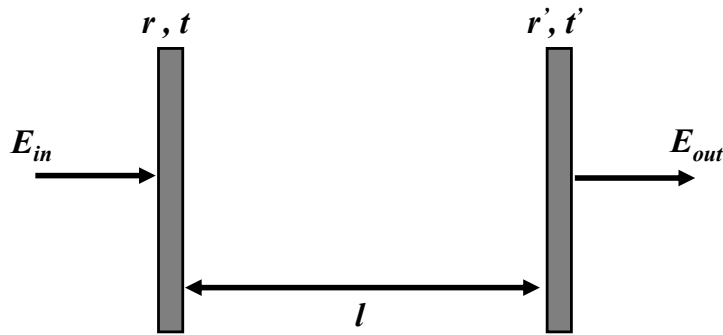


Figure 2: Sketch of a planar Fabry-Perot cavity.

The two mirrors are described by each their respective reflectivity r and transmission t and are placed parallel at a distance l from each other. The field at the second mirror, i.e. the transmitted field E_{out} can then be described as a function of the field at the first mirror, i.e. the incident field E_{in} [1][2]. The Fabry-Perot cavity furthermore gives rise to so-called eigenstates related to its length l , derived from considering the path difference between successive parallel beams through the cavity. Any allowed mode inside the cavity, and thus transmitted, must fulfill the brightness condition $2l = m\lambda$, where λ is the wavelength of the incident field and $m = 1, 2, 3, \dots$ is a positive integer.

2.1.1 Transmission

In order to determine the transmission through the Fabry-Perot cavity, we once again consider the configuration in figure 2. It is further, initially, assumed that the mirrors are both lossless, such that

$$|r|^2 + |t|^2 = |r'|^2 + |t'|^2 = 1. \quad (1)$$

This means that all losses, e.g. due to absorption or scattering, are neglected.

In order to formulate E_{out} in terms of E_{in} , we first consider the incident field as a propagating plane-wave

$$E_{in} = E_{0,in} e^{ik}, \quad (2)$$

where $k = 2\pi/\lambda$ is the wave number and $E_{0,in}$ is the amplitude of the field. We then consider E_{out} to be comprised of contributions for each roundtrip inside the cavity. This can be written as an infinite geometrical series given as

$$\begin{aligned} E_{out} &= tt' E_{0,in} e^{ik} + tt' E_{0,in} e^{ik} rr' e^{i\delta} \\ &\quad + tt' E_{0,in} e^{ik} (rr' e^{i\delta})^2 + tt' E_{0,in} e^{ik} (rr' e^{i\delta})^3 + \dots \\ &= tt' E_{0,in} e^{ik} \sum_{m=0}^{\infty} (rr' e^{i\delta})^m \end{aligned} \quad (3)$$

where $\delta = 2kl$. The first term of the series corresponds to a direct transmission through the cavity, and each term thereafter corresponds to the respective contribution to the transmission after the $m'th$ round trip.

By evaluating the series it is seen that it converges to the final expression for the transmitted field through a planar Fabry-Perot cavity found as

$$E_{out} = E_{0,in} \frac{tt' e^{i\delta/2}}{1 - rr' e^{i\delta}}. \quad (4)$$

The intensity of the transmission is now taken as the square of the norm of the field amplitude $|E_{out}|^2$ and normalizing with respect to the incident field intensity $|E_{0,in}|^2$. We arrive at an expression for the transmission intensity which is recognized to be given on the form of an *Airy function*[2]

$$T = \frac{|E_{out}|^2}{|E_{0,in}|^2} = \left| \frac{tt' e^{i\delta/2}}{1 - rr' e^{i\delta}} \right|^2 = \frac{(1 - |r|^2)(1 - |r'|^2)}{(1 - |rr'|)^2 + 4|rr'| \sin^2(\delta)}, \quad (5)$$

where δ is the phase shift associated with each round trip inside the cavity.

Figure 3 displays the Airy function in eq. (5), of a lossless cavity of reflectivities $r' = r$, as a function of δ in units of π . The function is plotted for the cases of $|r|^2 = 50\%$, shown in blue, and $|r|^2 = 90\%$, shown in red. It is readily seen that the transmission is maximized for $\delta = n2\pi$ and that the two cases shown differ significantly as the red profile is much narrower than the blue. The red profile

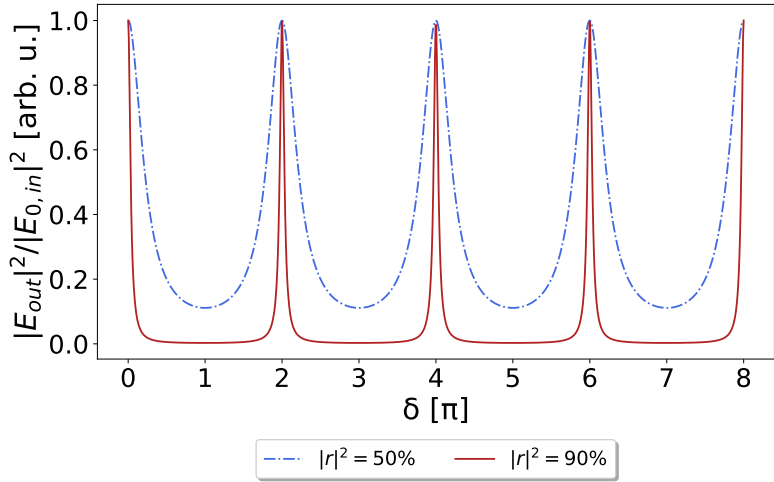


Figure 3: The red line shows the transmission spectrum of a *high* finesse Fabry-Perot cavity of reflectivity $|r|^2 = 0.90$, while the blue dashed line shows the transmission spectrum of a *low* finesse cavity with reflectivity $|r|^2 = 0.50$.

is hence said to have a higher *finesse* \mathcal{F} than the blue profile. The finesse is defined as

$$\mathcal{F} \equiv \frac{FSR}{\delta_\lambda}, \quad (6)$$

where *FSR* is the so-called *Free Spectral Range* indicating the spectral distance between two peaks and δ_λ refers to the *Full Width at Half Maximum (FWHM)* which, as the name suggests, is the linewidth defined at $T = 1/2$, i.e. at half the maximum value.

Considering the Airy function in eq. (5) for the high finesse case where $|r|^2 = |r'|^2 \rightarrow 1$ we furthermore see that each individual peak closely resembles a Lorentzian distribution.

2.1.2 Varying the cavity length

In order to relate the resonance transmission profile to the length of the cavity we first consider the frequencies at which the cavity is resonant, with respect to the incident light, given as

$$\nu_n = n \frac{c}{2l}, \quad (7)$$

where c is the speed of light, n is a positive integer referring to the order of the resonance frequency and l is the cavity length. This corresponds to resonance

occurring at times related to each round trip inside the cavity.

Since the FSR is defined as the spectral distance between each peak, it follows from eq. (7) that it can be expressed in units of frequency as

$$FSR_\nu = \frac{c}{2l}, \quad (8)$$

and the corresponding linewidth, or FWHM, δ_ν is then given as

$$\delta_\nu = \frac{1}{2\pi} \frac{|t|^2 + |t'|^2}{\tau}, \quad (9)$$

where $\tau = 2l/c$ is the round trip time in seconds.

Finally, considering the definition of the finesse from eq. (6) it can be shown that

$$\mathcal{F} \equiv \frac{FSR_\nu}{\delta_\nu} = \frac{2\pi}{|t|^2 + |t'|^2}, \quad (10)$$

where the finesse is now defined in terms of the total cavity transmission at resonance.

Note here that the relation between the FSR and the cavity length l is clearly shown in eq. (8), and figure 4 furthermore shows transmission spectra underlining the effect of changing the cavity length.

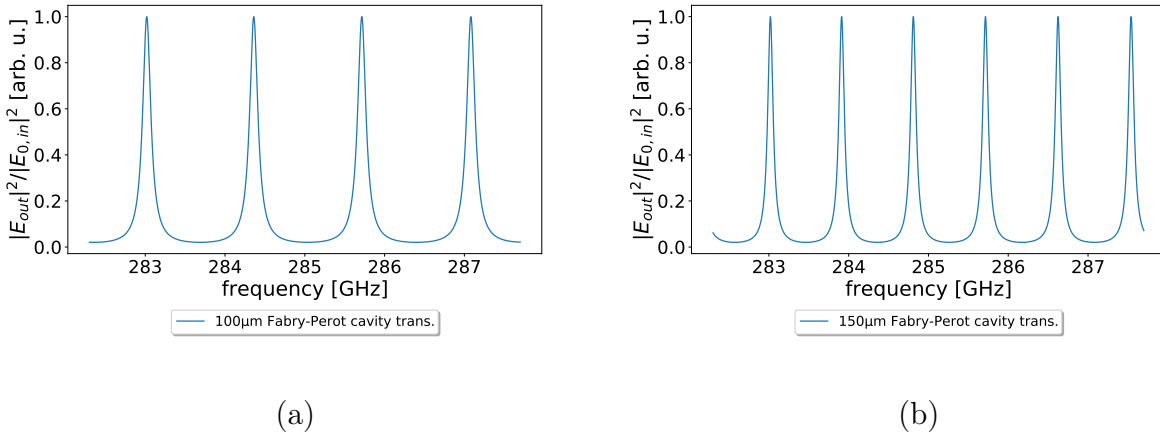


Figure 4: (a) shows the transmission spectrum of a Fabry-Perot cavity of length $l \approx 100\mu m$ as a function of the frequency ν , while (b) shows the transmission spectrum of a cavity of length $l \approx 150\mu m$ for the same range of frequencies. Note here how the FSR is inversely proportional to the cavity length.

2.1.3 Varying the incident wavelength

In order to simplify the Airy function in eq. (5) we introduce the so-called *coefficient of finesse* F , which is a function only of the mirror reflectivities, given as

$$F = \frac{4|rr'|}{(1 - |rr'|)^2}. \quad (11)$$

The coefficient of finesse F is not to be confused with the finesse \mathcal{F} . While the finesse is related to the sharpness of the transmission peaks, the coefficient of finesse refers to the contrast of the peaks in the sense that the difference between the minimum and maximum transmittance level increases with F . The coefficient of finesse is related to the finesse as

$$\mathcal{F} = \frac{\pi}{2}\sqrt{F}. \quad (12)$$

Rewriting the Airy function in terms of the coefficient of finesse yields

$$T_\lambda = \frac{1}{1 + F\sin^2(\delta/2)}, \quad (13)$$

where the round trip phase shift δ is related to the wavelength λ of the incident light by

$$\delta = 2kl = \frac{4\pi l}{\lambda}, \quad (14)$$

as $k = 2\pi/\lambda$ is the incident wave number.

Re-writing the general cavity brightness condition, it can be shown that the resonant wavelengths for a cavity at normal incidence are given as

$$\lambda_n = \frac{2l}{n}, \quad (15)$$

where $n = 1, 2, 3, \dots$ is a positive integer referring to the order of the resonance.

Since $\nu = c/\lambda$, the relation between the linewidth in wavelength space δ_λ and the one in frequency space δ_ν is non-linear. Therefore one does not simply make the aforementioned substitution in order to relate them. It can however be shown that their respective expressions differ by a factor of λ^2/c , and the linewidth when varying the wavelength is thus given as

$$\delta_\lambda = \frac{\lambda^2}{c} \cdot \delta_\nu = \frac{\lambda^2}{4\pi l}(|t|^2 + |t'|^2). \quad (16)$$

Finally we consider the definition for the finesse \mathcal{F} and the expression given in eq. (10), in order to show that the FSR in wavelength space is given as

$$FSR_\lambda \equiv \delta_\lambda \cdot \mathcal{F} = \frac{\lambda^2}{2l}. \quad (17)$$

Figure 5 shows an example of the Airy function given in eq. (13) as a function of the wavelength for a Fabry-Perot cavity of reflectivities $|r|^2 = |r'|^2 = 90\%$ and length $l = 100\mu m$.

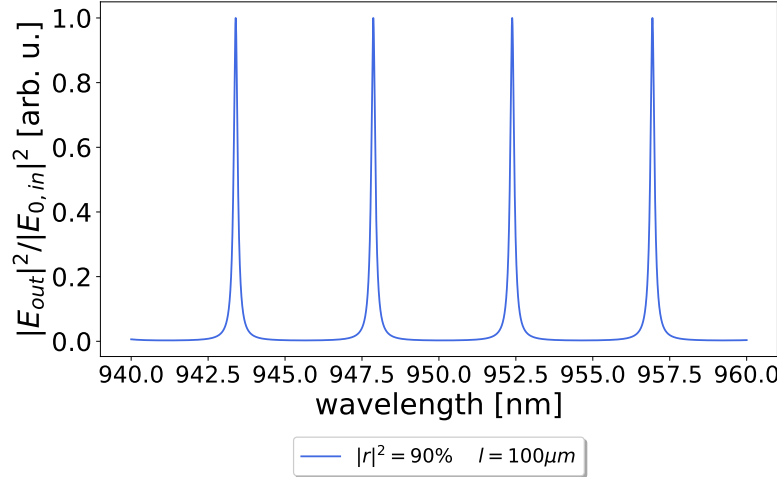


Figure 5

2.1.4 Cavity losses

In eq. (10) we assume the case of a lossless cavity, i.e. eq. (1) is fulfilled. In practice, any cavity will have some amount of losses, which would have to be taken into account when calculating the finesse. When losses are present eq. (1) instead generally reads

$$|r|^2 + |t|^2 + L + L' = 1, \quad (18)$$

where L and L' indicates the fractional losses of each mirror.

In this case the finesse would be given as

$$\mathcal{F} = \frac{2\pi}{|t|^2 + |t'|^2 + L_{total}}, \quad (19)$$

where $L_{total} = L + L'$ are the total additional cavity losses.

The effect on the transmission spectrum of a cavity with losses is that the level of the normalized transmission will not reach unity, as some light is lost to e.g. absorption or scattering for each round trip of the cavity.

2.2 The Fano mirror: a sub wavelength grating

2.2.1 Reflection/transmission spectra and line shape analysis

2.2.2 Lossless grating

We wish to analytically describe the wavelength-dependent spectra for the transmission and reflectivity of an infinite sub-wavelength grating. The wavelength dependence arises from the fact that any incident light will be subject to interactions with the so-called *guided-mode* of the grating. The grating is, in this way, said to act as an effective TM_0 waveguide, ensuring resonant modes will only be reflected in the 0'th order.

By first considering the case where absorption and thermal coupling effects are neglected, i.e. a lossless grating, we can assume conservation of energy and thereby the relations

$$|r_g|^2 + |t_g|^2 = 1 \quad \text{and} \quad |r_d|^2 + |t_d|^2 = 1, \quad (20)$$

where the subscripts g and d indicate the *grating* and *direct* transmissions and reflectivities, respectively. It is implied that the direct coefficients are constants and describe the transmission and reflectivity when the incident wavelength is significantly detuned from any guided-mode resonance of the grating. Furthermore, it is also implied that the grating coefficients are functions of the incident wavelength.

We now assume a normal incident beam on the grating as a linearly polarized monochromatic plane wave, with a wavelength close to a guided-mode resonance of the grating. In order to describe the coefficients r_g and t_g we follow the formalism presented by Fan and Joannopoulos [3] and consider the likely paths of the incident light through the grating. It is quite intuitive to consider the case where the light is simply transmitted, and this shall be our first case hereafter denoted the *direct pathway*. Another case one might consider is the one where the incident light excites the guided-mode resonance in the grating. This case is denoted the *indirect pathway* and decays more slowly than its direct counterpart.

The interference caused when the guided mode is excited is often referred to as *Fano resonances*, due to its physical similarities to the description of interference between a discrete autoionized state and a bound continuum state first reported by Fano [4]. The cross section of inelastic scattering, when measured as a function of energy, showed characteristic asymmetric peaks. These were described as

the aforementioned interference pattern between *direct* (the discrete state) and *indirect* (the continuum state) pathways.

By generalizing the model of Fan and Joannopoulos [3] we describe the transmission and reflectivity coefficient amplitudes as

$$r_g = r_d + \frac{a}{k - k_1 + i\gamma} \quad \text{and} \quad t_g = t_d + \frac{b}{k - k_1 + i\gamma}, \quad (21)$$

where $k = 2\pi/\lambda$ is the incident wave number, $k_1 = 2\pi/\lambda_1$ is the wave number according to the guided-mode resonance and γ is the HWHM (half width at half maximum) of the guided-mode resonance. Complex coefficients a and b describe the interference between the directly transmitted or reflected waves and the guided mode of the grating.

Note that in eq. (21) the right side of the expression for each coefficient corresponds to the continuum state i.e. the indirect pathway, while the direct transmission and reflection coefficients take the role of the autoionized discrete state, i.e. the direct pathway[4].

As we are dealing with an ideal, lossless, grating, we assume coefficients a and b to be equal, meaning that we specifically assume vertical symmetry throughout the grating. By considering eq. (20) this in turn leads to

$$a = b = -i\gamma(t_d + r_d), \quad (22)$$

which further yields an expression for the grating transmission amplitude coefficient on the form

$$t_g = t_d \frac{k - k_0}{k - k_1 + i\gamma}. \quad (23)$$

Here, the newly introduced $k_0 = 2\pi/\lambda_0 = k_1 - i\gamma(r_d/t_d)$ is the zero-transmission/unity-reflectivity wave number.

To generalize eq. (23) to include non-unity reflectivity and non-zero transmission, we allow for $a \neq b$ [5][6][7], meaning that the case of vertical asymmetry is included in the model[8]. By assuming $r_d, t_d \in \mathbb{R}$, eq. (20) leads to the coupled differential equations

$$\begin{aligned} t_d x_a + r_d x_b &= 0, \quad \text{and} \\ x_a^2 + y_a^2 + x_b^2 + y_b^2 + 2t_d\gamma y_a + 2r_d\gamma y_b &= 0, \end{aligned} \quad (24)$$

where $\{x, y\}_{a,b}$ respectively denotes the real and imaginary parts of the coefficients a and b . Solving eqs. (24) leads to the correct complex reflectivity

coefficients and the expression for the transmission coefficient amplitudes now reads

$$t_g = t_d \frac{k - k_0 + i\beta}{k - k_1 + i\gamma}, \quad (25)$$

where k_0 and β are defined from the expression for a found by solving eqs. (24), given as

$$a = t_d(k_1 - k_0 - i\gamma + i\beta). \quad (26)$$

Finally, this allows for non-zero transmission and non-unity reflectivity at wave number k_0 .

To show the validity of the model at this point, we introduce a periodic grating which is arbitrarily sketched in figure 6. The sketch indicates the period of the grating Λ , the top finger width w_t , the offset between the finger top and the bottom of the grating x , the total grating thickness t and finger depth d . Furthermore, the grating is patterned in a *silicon nitride (SiN)* membrane of refractive index n_{SiN} .

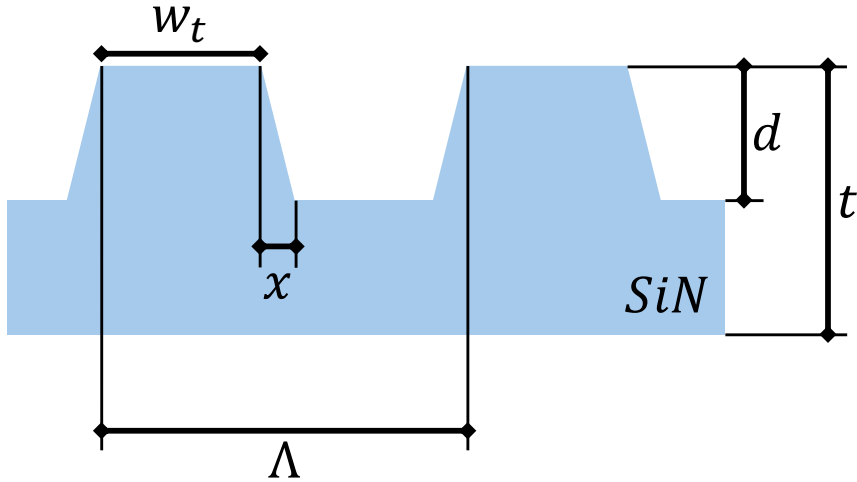


Figure 6: Schematics of a periodic optical *SiN* grating with physical parameters: $\Lambda = 857\text{nm}$, $w_t = 623\text{nm}$, $h = 55.1\text{nm}$, $t = 152\text{nm}$, $d = 67\text{nm}$, $n_{SiN} = 2.15$.

In order to simulate the transmission and reflectivity profiles as a function of the incident wavelength, we utilize the *Modeled Integrated Scatter Tool (MIST)* developed by the *National Institute of Standards and Technology (NIST)*[9]. The simulation solves Maxwell's equations for any pre-defined infinite periodic structure.

MIST assumes an incident plane-wave, and hence predicts the *ideal* spectra for the transmission and reflectivity, i.e. zero and unity when on resonance,

respectively. In order to include effects related to the Gaussian behaviour of a more realistic incident beam, such as collimation and finite-size effects[10], one would have to solve Maxwell's equations for a Gaussian distribution. We safely assume an incident plane-wave for reasons related to the order of magnitude for the *Rayleigh range* of the beam used, compared with that of the spacial range of the conducted experiments.

In reality, the interference inside the cavity however cannot be perfect, as any Gaussian beam can be represented by a number rays, infinitesimal in size, which would all track differently through the grating, resulting in non-unity reflectivity and non-zero transmission. In order to synthetically correct for this we scale each transmission value found by MIST according to

$$t_g = (1 - \varepsilon) \cdot t_{MIST} + \varepsilon, \quad (27)$$

where we define the correction to be arbitrarily small as $\varepsilon = 1\%$.

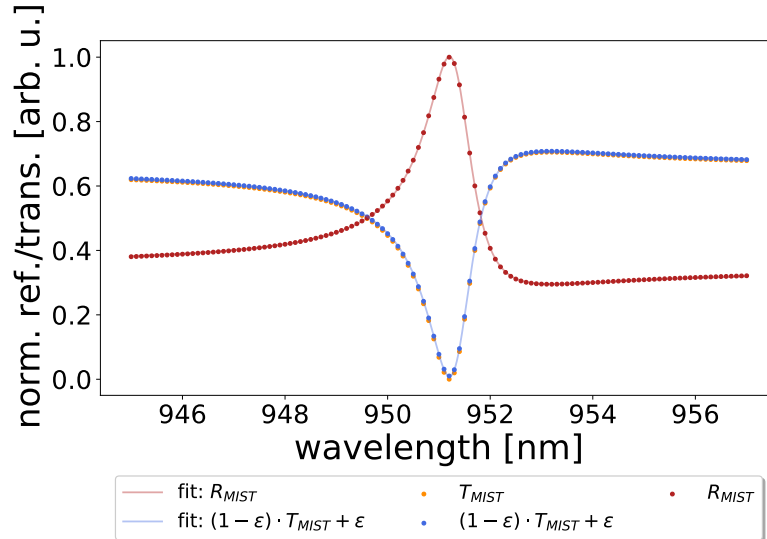


Figure 7: Reflectivity and transmission values (scaled and unscaled) found from a MIST simulation plotted with the corresponding least squares fit to the model in eq. (25). The resulting grating parameters are given as $\lambda_0 = 951.208\text{nm}$, $\lambda_1 = 951.356\text{nm}$, $t_d = 80.94\%$, $r_d = 52.7\%$, $\gamma_\lambda = 0.527$, and $\beta = 4.42 \cdot 10^{-7}$.

Figure 7 shows the scaled and unscaled results of the simulation using MIST for the following physical grating parameters:

$$\begin{aligned} \Lambda &= 857\text{nm}, \quad w_t = 623\text{nm}, \quad h = 55.1\text{nm}, \\ t &= 152\text{nm}, \quad d = 67\text{nm} \quad \text{and} \quad n_{SiN} = 2.15, \end{aligned} \quad (28)$$

The reflectivity- and (corrected) transmission values were then fitted to the model in eq. (25) using a least squares fitting method, and plotted along with the simulated values. The resulting grating parameters were found as

$$\begin{aligned}\lambda_0 &= 951.208\text{nm}, \quad \lambda_1 = 951.356\text{nm}, \quad t_d = 80.94\%, \\ r_d &= 52.7\%, \quad \gamma_\lambda = 0.527\text{nm} \quad \text{and} \quad \beta = 4.42 \cdot 10^{-7},\end{aligned}\tag{29}$$

where λ_0 is the cavity mode resonance wavelength, λ_1 is the guided-mode resonance wavelength, r_d (t_d) is the direct reflectivity (transmission), γ_λ is the width of the guided-mode resonance and β is a constant associated with non-unity reflectivity and non-zero transmission.

2.2.3 Lossy grating

In order to modify the above model such that losses, e.g. due to absorption or thermal coupling effects, are accounted for, we add a resonant loss term to the energy conservation relation in eq. (20). For this we introduce the resonant loss level L , which must be known in order to accurately calculate the complex reflectivity coefficients. The energy conservation relation is modified such that

$$|t_g|^2 + |r_g|^2 + \frac{c^2}{(k - k_1)^2 + \gamma^2} = 1,\tag{30}$$

where the coefficient $c^2 = L((k - k_1)^2 + \gamma^2)$ includes the resonant loss term L . A new set of coupled differential equations are found, using eq. (30), given as

$$\begin{aligned}t_d x_a + r_d x_b &= 0, \quad \text{and} \\ x_a^2 + y_a^2 + x_b^2 + y_b^2 + c^2 + 2t_d \gamma y_a + 2r_d \gamma y_b &= 0.\end{aligned}\tag{31}$$

It is easily identified that eq. (24) and eq. (31) differ only by the addition of coefficient c^2 , and thereby the losses. Solving eq. (31) leads to the correct complex reflectivity coefficients, except that they now account for any losses associated with the grating.

In conclusion, the complete grating model consists of an expression for the transmission coefficients and a set of coupled differential equations for the reflection coefficients, shown in eq. (25) and eq. (31), respectively. The model on the form used for this project and subsequent thesis is derived in previous work by A. Darki et al. [11] and more recently T. Mitra et al. [12].

Figure 8 shows reflection and transmission spectra of a grating of parameters given in eq. 29 with a synthetic non-zero resonance loss term in order to show

the effect of including losses. It is seen from the added *loss curve* that the losses increase when approaching the resonance wavelength, as the interaction with the guided-mode, and thus the grating, gets stronger in this region.

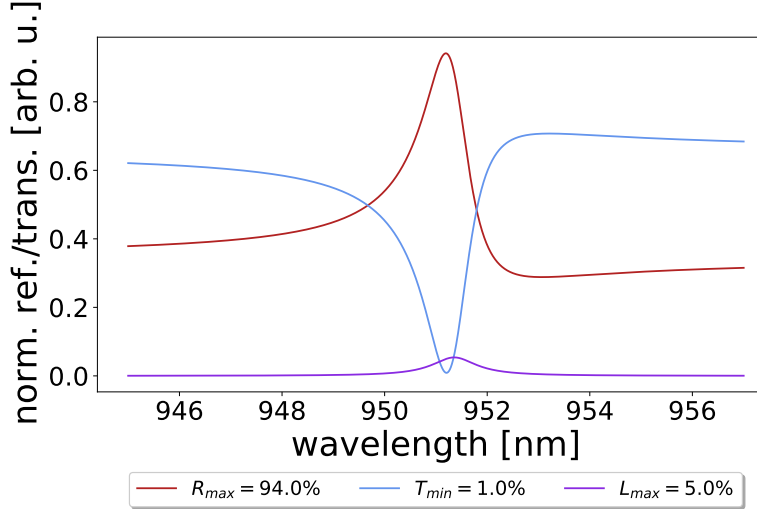


Figure 8: Simulated reflectivity and transmission spectra of a grating of parameters given in eq. (29) with a synthetically added non-zero loss term, and the corresponding grating losses.

2.3 The single Fano cavity

2.3.1 The single Fano cavity model

The single Fano cavity consists of a planar broadband mirror, and a sub-wavelength grating, i.e. a Fano mirror, as described in section 2.2 and seen in figure 9 where schematics of the single Fano and broadband cavity configurations are shown. While the broadband mirror has fixed optical properties, the Fano mirror has transmission and reflection coefficients dependent on the incident wavelength, according to solutions to the coupled differential equations of eq. (31).

In order to model the single Fano cavity transmission spectra, we therefore consider the transmission function of a normal incident and planar Fabry-Perot cavity in eq. (4) with $r, t \rightarrow r_m, t_m$ and $r', t' \rightarrow r_g(\lambda), t_g(\lambda)$ [13]. Here the subscript m indicates the broadband *mirror* coefficients, and g is for *grating*, which indicates the coefficients of the Fano mirror. Rewriting eq. (4) such that

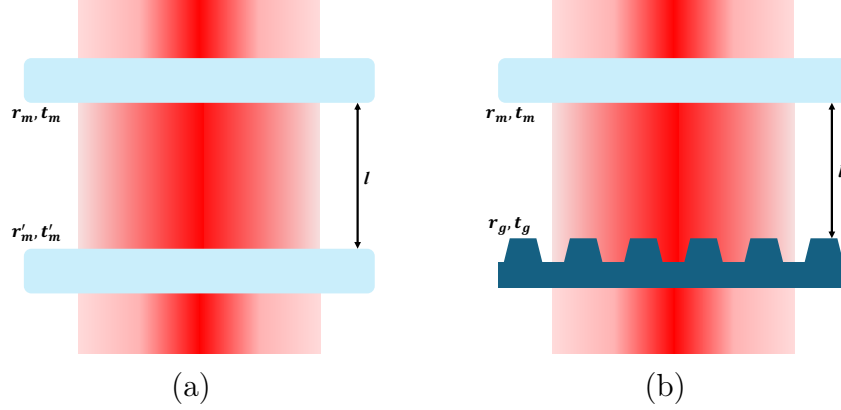


Figure 9: In (a) is seen the schematics of a cavity consisting of two broadband mirrors with transmission and reflectivity coefficients t_m , r_m , t'_m , and r'_m . (b) shows the schematics of a single Fano cavity consisting of one broadband mirror with coefficients t_m , r_m and one Fano mirror with wavelength dependent coefficients t_g , r_g . The reflectors in either cavity are separated by a cavity length l .

it describes the normalized transmission amplitude, through the single Fano cavity, $T_{cav} = |E_{out}|^2 / |E_{0,in}|^2$ we get

$$T_{cav} = \left| \frac{t_m t_g(\lambda) e^{i\phi}}{1 - r_m r_g e^{2i\phi}} \right|^2, \quad (32)$$

where $\phi = 2\delta = kl$, $k = 2\pi/\lambda$ and l is the cavity length, as is consistent the general case described in section 2.2.

2.3.2 Transmission linewidth

In order to analytically describe how the transmission spectrum at, or close to, the overall resonance¹ behaves as a function of the incident wavelength, we attempt to generalize the Fano model for this specific scenario. Considering the case where the cavity resonance closely resembles the guided-mode resonance of the Fano mirror (the zero-transmission wavelength), eq. (32) can be approximated well by

$$T_{cav} \approx \frac{A}{1 + \left(\frac{\Delta}{1 - \nu \Delta} \right)^2}, \quad (33)$$

¹This terminology is used for the scenario where the guided-mode, cavity mode and input laser mode all meet the resonance condition $\lambda_g \approx \lambda_c \approx \lambda_l$, where g, c, l stands for grating/guided-mode, cavity and laser, respectively.

where $\Delta = (\lambda - \lambda_c)/\delta\lambda$ is the detuning from the cavity resonance normalized by the HWHM $\delta\lambda$, and ν is a constant describing the asymmetry of the single Fano transmission spectrum. [12][11]

From eq. (33) it can be shown that the HWHM of the Fano transmission profile around the overall resonance wavelength, i.e. when $\lambda_c \approx \lambda_0$, is approximately given as

$$\delta\lambda \approx \frac{1}{\frac{1}{\delta\lambda_c} + \frac{1}{\delta\lambda_g}}, \quad (34)$$

where

$$\delta\lambda_c = \frac{\lambda_0^2}{8\pi l} (|t_g(\lambda_0)|^2 + |t_m|^2 + L) \quad (35)$$

is the HWHM of a broadband cavity and

$$\delta\lambda_g = \frac{\gamma\lambda}{2(1 - r_d)} (|t_g(\lambda_0)|^2 + |t_m|^2 + L) \quad (36)$$

is the HWHM of the Fano cavity in the so-called Fano regime.[12][11] In eqs. (34)-(36) λ_0 is the Fano cavity resonance wavelength, l is the cavity length, $L = (1 - |r_g(\lambda_0)|^2 - |t_g(\lambda_0)|^2)$ is the total additional losses of the cavity when on resonance, $\gamma\lambda$ is the width of the guided-mode resonance of the Fano mirror and r_d is the off-resonance, or *direct*, reflectivity of the Fano mirror.

The *Fano regime* and its counterpart the so-called *standard regime* are defined for a given single Fano cavity, by its length l . By inspection of eqs. (35) and (36) it is seen that for $l \rightarrow \infty$ the linewidth in eq. (34) is dominated by the broadband cavity term, while for the opposite case, $l \rightarrow 0$, the linewidth is predominantly given by the Fano cavity term.

Generally the Fano regime describes the cavity lengths for which eq. (34) shows a significant divergence from the broadband linewidth in eq. (35). Oppositely, when in the standard regime the broadband and Fano cavity produces resonance transmission peaks of comparable, if not equal, linewidths.

Figures 10a and 10b depicts two examples, in each their regime, of single Fano cavity transmission spectra together with their respective complimentary broadband cavity transmission profiles, and the reflectiviy amplitude of the Fano mirror used to model both profiles. As shown in section 2.2 any Fano mirror, or grating, is described by five characterizing parameters. For the one

used to model the transmission spectra in figures 10a and 10b these are

$$\begin{aligned} \lambda_0 &= 951\text{nm}, \quad \lambda_1 = 951\text{nm}, \quad t_d = 80\%, \\ \gamma\lambda &= 0.5\text{nm} \quad \text{and} \quad \beta = 0, \end{aligned} \quad (37)$$

where we remember that $\lambda_{0,1}$ are the resonant wavelengths for, respectively, the cavity- and guided-modes, t_d is the direct transmission, $\gamma\lambda$ is the width of the guided-mode resonance and β is a constant describing the losses of the grating, which here are set to 0, and thus neglected. The broadband mirror parameters are chosen such that they perfectly resemble the transmission and reflectivity of the Fano mirror on resonance, which is arbitrarily chosen such that $|r_m|^2 = 95\%$ and $|t_m|^2 = 5\%$.

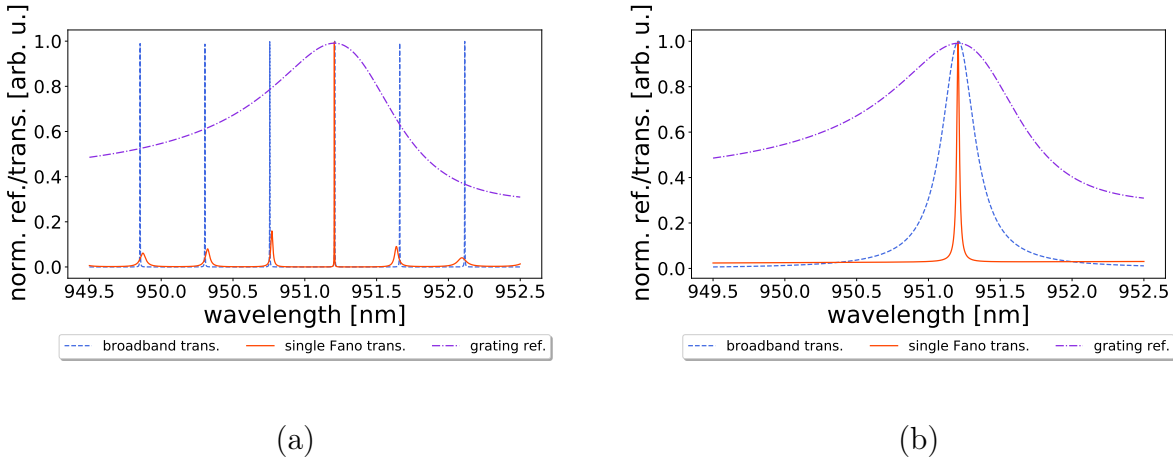


Figure 10: In (a) is seen the comparison of broadband and single Fano cavity transmission spectra for a cavity length of $l \approx 1000\mu\text{m}$, i.e. in the *standard* regime. (b) shows the same comparison, but for a cavity length of $l \approx 5\mu\text{m}$, i.e. in the so-called *Fano* regime.

Figure 10a shows the transmission spectra of the two cavities for a length of $l \approx 1000\mu\text{m}$, i.e. in the standard regime. It is clear from inspection of the figure that the resonance transmission profile of the standard broadband cavity is not wavelength dependent, in the sense that all fringes appear to have the same high finesse \mathcal{F} , i.e. ratio between the FSR and HWHM. This is not the case for the Fano cavity which is due to the wavelength dependence of the optical properties of the Fano mirror, as this causes the transmission and reflectivity to *only* match those of the broadband mirror when on resonance. Furthermore, no significant difference in linewidth is seen for the transmission of the two cavities on resonance, as predicted by eq. (34).

In figure 10b, the transmission spectra of both cavities are shown for a length of $l \approx 5\mu m$, i.e. in the Fano regime, where it is clearly seen that while the standard cavity experiences broadening for shorter cavity lengths², this is not the case for the Fano cavity transmission peak.

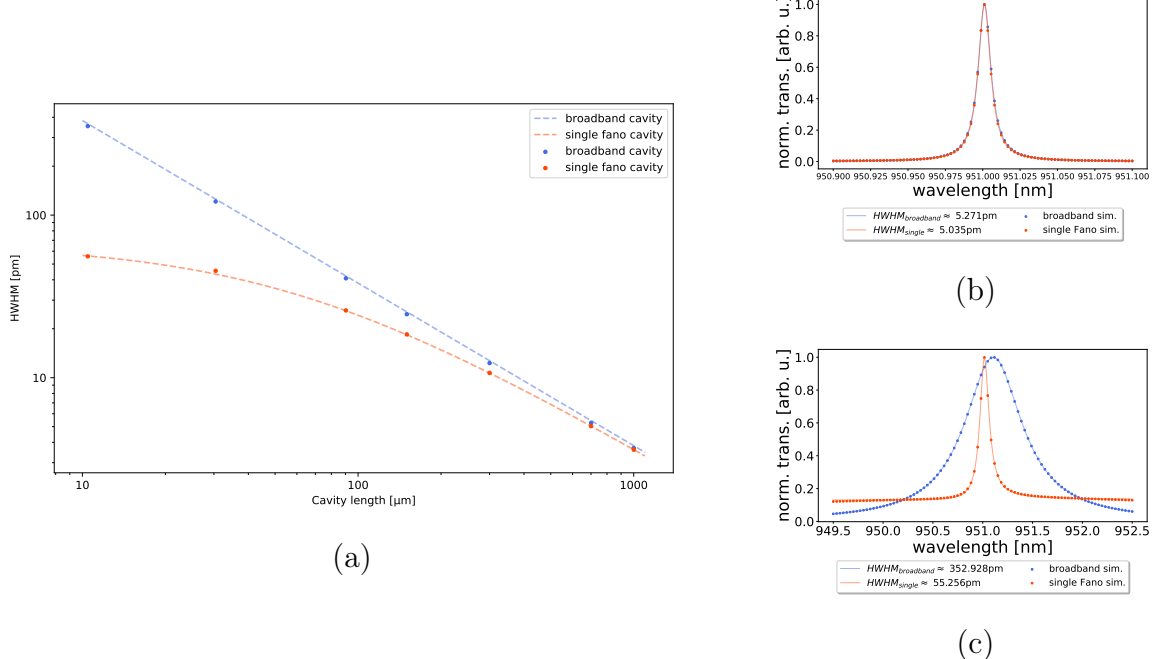


Figure 11: (a) shows the approximate analytical resonance linewidths (eq. (34)) as a function of cavity length for the broadband and single Fano cavities together with linewidths of transmission profiles simulated using eq. (32) and eq. (4), found as parameters of least squares fits, for comparison. In (b) and (c) is seen transmission spectra of broadband and single Fano cavities of lengths $\sim 700\mu m$ and $\sim 10\mu m$, respectively. The spectra shown indicate each their respective linewidths, and are examples of the values plotted in (a).

Figure 11a models the behavior of the linewidth of the single Fano cavity compared with the one for a broadband cavity of similar optical properties, as a function of wavelength. Here it is easily seen where the linewidth of the single Fano transmission begins to saturate, and hence deviate from the one of the broadband cavity. The plotted line in the figure is calculated using eq. (34) while the points depict linewidths found as a fitting parameter from a least squares fit of the general Fano model in eq. (33) to transmission spectra simulated by

²This is a natural consequence of the shorter cavity as this causes the lifetime inside the cavity to fall and hence the transmission HWHM to rise. The HWHM is inversely proportional to the lifetime and goes as $\delta\lambda \propto 1/\tau$.

the Fabry-Perot (eq. (4)) and single Fano (eq. (32)) transmission functions. Finally, it can be concluded that the approximate analytical expression for the linewidth of the broadband and single fano cavities in eq. (34) correlates very well with the values found from the simulated spectra.

2.4 The double Fano cavity

2.4.1 The double Fano cavity model

While the single Fano cavity is usually known in the appropriate litterature as simply a *Fano cavity*, I have insisted on including the fact that it contains only one Fano mirror, and hence denoted it the *single* Fano cavity. This addition is justified by the contents of this section, and namely that we now move on to the *double* Fano cavity, which as the name suggests consists of two Fano mirrors. The schematics of this configuration is shown together with the one for the single Fano cavity in figure 12.

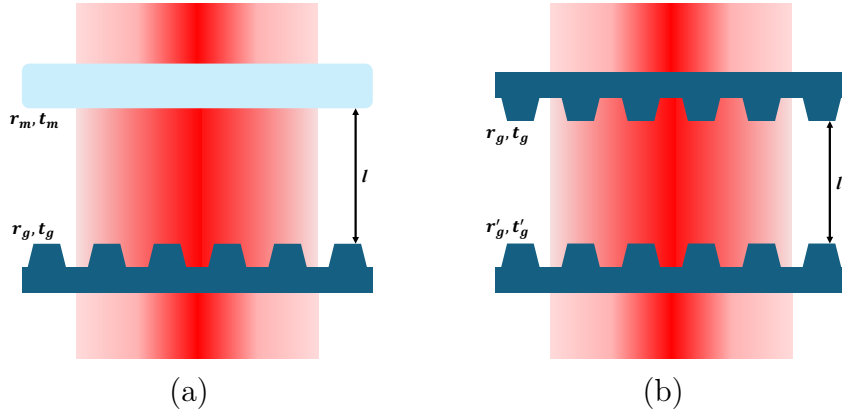


Figure 12: (a) shows schematics of the single Fano cavity consisting of a broadband mirror with transmission and reflectivity coefficients t_m , r_m and a Fano mirror with coefficients t_g , r_g . (b) shows the schematics of the double Fano cavity consisting of two Fano mirrors with coefficients t_g , r_g , t'_g , r'_g . Both cavities are separated by a cavity length l .

Here it is evident that instead of having one set of reflectivity and transmission coefficients that depend on the incident wavelength, we now have two. In order to model the transmission of the double Fano cavity, we once again consider the transmission function for the normal incident and planar Fabry-Perot cavity in eq. (4), this time with $r, t \rightarrow r_g(\lambda), t_g(\lambda)$ and $r', t' \rightarrow r'_g(\lambda), t'_g(\lambda)$ [13]. We rewrite the Fabry-Perot transmission function with the addressed substitutions of the optical coefficients and such that it decribes the normalized transmission

amplitudes $T_{cav} = |E_{out}|^2/|E_{0,in}|^2$ and get

$$T_{cav} = \frac{t_g(\lambda)t'_g(\lambda)e^{i\phi}}{1 - r_g(\lambda)r'_g(\lambda)e^{2i\phi}}. \quad (38)$$

The subscript g indicates a grating transmission or reflectivity. Figure 13 shows an example of the normalized transmission spectrum of an $\sim 30\mu m$ double Fano cavity on- and off-resonance, found using eq. (38).

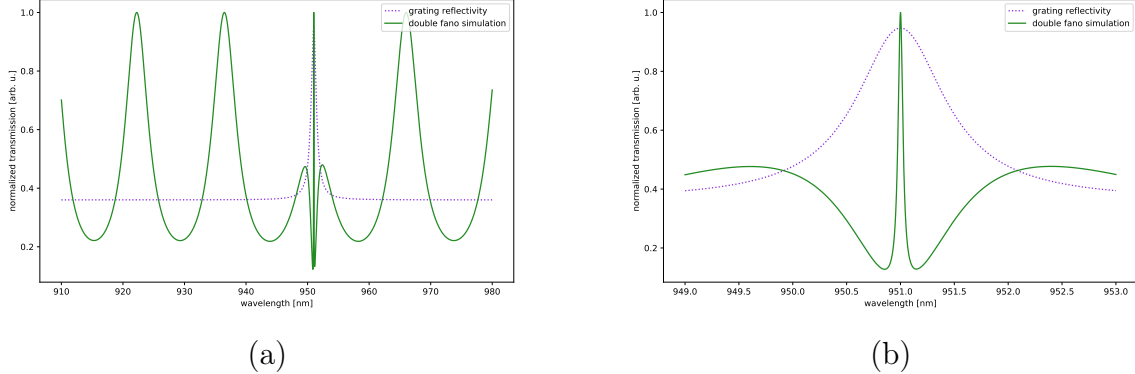


Figure 13: An example of a normalized double Fano transmission spectrum of an $\sim 30\mu m$ cavity. (a) shows a long-range wavelength scan, depicting both the on- and off-resonance behaviour of the double Fano cavity transmission, while (b) shows the transmission focussed specifically around the resonance position. Both examples are shown together with the reflectivity of the Fano mirror used to model them.

2.4.2 Transmission linewidth

In order to describe the analytical linewidth of the transmission profile of the double Fano cavity, we take a similar approach as in the single Fano case outlined in section 2.3.2. It can be shown from eq. (34) when including the wavelength dependence of the optical coefficients of both Fano mirrors, that the HWHM $\delta\lambda$ of the double Fano cavity transmission profile is approximately given as

$$\delta\lambda^{double} \approx \frac{1}{\frac{1}{\delta\lambda_c} + \frac{1}{\delta\lambda_g^{double}}}, \quad (39)$$

where

$$\delta\lambda_c = \frac{\lambda_0^2}{8\pi l}(|t_g(\lambda_0)|^2 + |t'_g(\lambda_0)|^2 + L) \quad (40)$$

is still the HWHM of a broadband cavity and

$$\delta\lambda_g^{double} = \frac{\gamma\lambda}{4(1-r_d)}(|t_g(\lambda_0)|^2 + |t'_g(\lambda_0)|^2 + L). \quad (41)$$

is the HWHM of the double Fano cavity in the Fano regime. Note that $\delta\lambda^{double} = \delta\lambda^{single}/2$ for $l \rightarrow 0$ when eq. (39) is predominantly given by eq. (41). In this brief evaluation of the estimated analytical linewidth of the double Fano transmission profile it is assumed that all defining parameters of the two Fano mirrors are identical, except for the cavity and guided-mode resonance wavelengths $\lambda_{0,1}$. Namely the following relevant parameters are assumed identical,

$$r_d = r'_d \text{ and } \gamma\lambda = \gamma\lambda'. \quad (42)$$

In this way any spectral detuning of the two Fano mirrors used to make a cavity is included in the analytical expression. The spectral detuning, and the effect hereof, will be further described in section 2.4.5.

2.4.3 Single and double Fano cavity comparison

Using the analytical expression for the double Fano cavity transmission in eq. (39) we are now in a position to compare the single and double Fano cavities. Note that we at this point only consider the ideal case of the double Fano cavity where additional cavity losses are neglected and the two Fano mirrors used are identical, i.e. the cavity is said to be *symmetrical*. The additional cavity losses are explicitly set to be given as

$$L = 1 - |r_g|^2 - |t_g|^2 = 0. \quad (43)$$

Figure 14 shows the transmission of the ideal double Fano cavity and the corresponding single Fano cavity for comparison.

Figure 14a shows the transmission for a cavity length of $\sim 1000\mu m$ which is well-inside the standard regime outlined in section 2.3.2 where the standard broadband and single Fano cavities produce transmission spectra of roughly identical linewidths. In this regime, due to the $1/l$ proportionality of the FSR, the off-resonance behavior of the double Fano cavity transmission is visible in the range plottet. It is seen, contrary to the single Fano cavity, that the transmission at each cavity resonance reaches a normalized transmission of $|E_{out}|^2/|E_{0,in}|^2 = 1$. This is due to the fact that the two gratings, while they

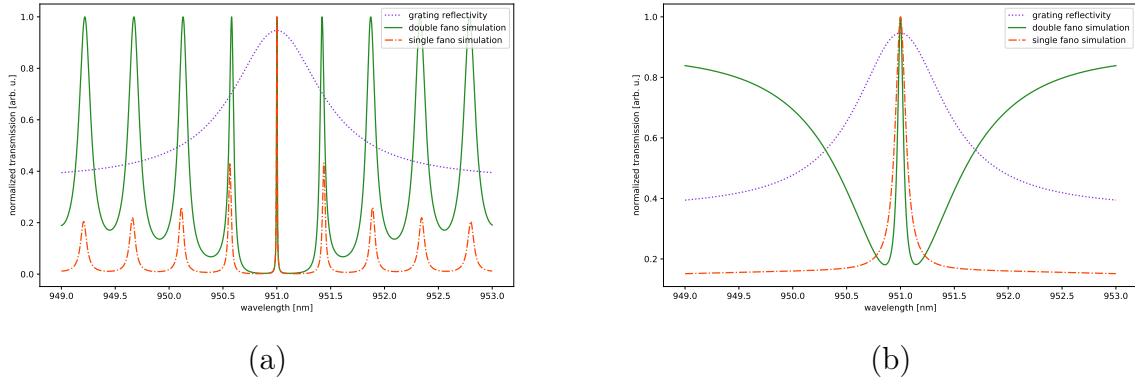


Figure 14: Comparison of the single and double Fano transmission spectra in the *standard* and *Fano* regimes. (a) shows the spectral comparison for an $\sim 1000\mu\text{m}$ cavity, i.e. in the *standard* regime, while (b) shows the same for an $\sim 5\mu\text{m}$ cavity, i.e. in the *Fano* regime. The Fano mirror reflectivity is depicted in both (a) and (b).

have wavelength dependent transmission and reflectivity coefficients, always have identical ones for the ideal case, which maximizes the Fabry-Perot transmission function and ensures unity transmission at any cavity resonance. The minimum level of the cavity changes according to the reflectivity of the Fano mirrors and by that the HWHM also changes as we move further from the guided-mode resonance. Both the minimum transmission level and the HWHM converge when moving away from the resonance wavelength, when the reflectivity becomes constant.

Figure 14b shows the transmission of a double Fano cavity of length $\sim 5\mu\text{m}$ which, contrary to the one in figure 14a, is well within the Fano regime. It is seen that the double Fano cavity transmission produces a resonance peak with a HWHM narrower than the one for the single Fano cavity, as is predicted in eq. (41). Furthermore, the immediate off-resonance behavior of the double Fano cavity transmission in the Fano regime, is drastically different than for the single Fano cavity. This is due to the collective higher transmission in this region compared with the single Fano case where the broadband mirror has a constant, and often high, reflectivity and hence a correspondingly low transmission.

Figure 15a shows the analytical linewidth calculated and compared for the broadband, single Fano, and double Fano cavities, calculated using eqs. (35), (34), (39). These are compared with linewidths found as fitting parameters from a least squares fit of the general Fano transmission formula given in eq. (33) to

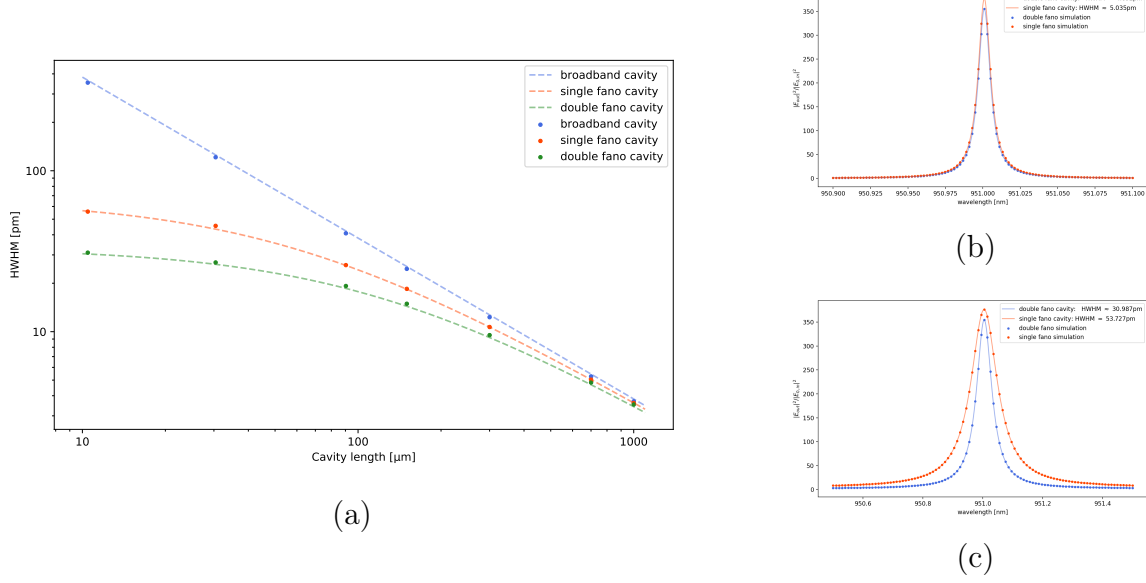


Figure 15: (a) shows the analytical resonance linewidths (eqs. (34), (39), and (35)) as a function of the cavity length for the broadband, single and double Fano cavities together with linewidths of corresponding profiles simulated using eqs. (32), (38), and (4) for comparison. In (b) and (c) is seen intracavity spectra of single and double Fano cavities of lengths $\sim 700\mu m$, and $\sim 10\mu m$, respectively. The spectra shown indicate each their respective linewidths, and are examples of the values plotted in (a). Note however, that the broadband cavity peak has been left out of (b) and (c).

transmission spectra calculated using eqs. (4), (32), and (38). According to eq. (39) the linewidth of the double Fano cavity transmission should converge to exactly half that of the single Fano cavity, meaning that

$$\delta\lambda_{double} = \frac{\delta\lambda_{single}}{2}, \quad \text{for } l \rightarrow 0. \quad (44)$$

This is supported well by the simulation depicted in figure 15a.

Figures 15b and 15c contain examples of intracavity³ spectra of single and double Fano cavities and corresponding least squares fits to the general Fano model in order to determine their linewidths.

³The reason these are shown as intracavity spectra instead of transmission spectra is due to the immediate off-resonance behavior of the double Fano cavity transmission. The shape makes accurate fitting a challenge, and while the intracavity spectra cannot be measured in the lab, the linewidth when simulated is identical to the resulting transmission peaks.

2.4.4 Additional cavity losses

Thus far we have only examined a lossless double Fano cavity where

$$|r_g|^2 + |t_g|^2 = 1 \quad (45)$$

is fulfilled for both Fano mirrors used to construct the cavity.

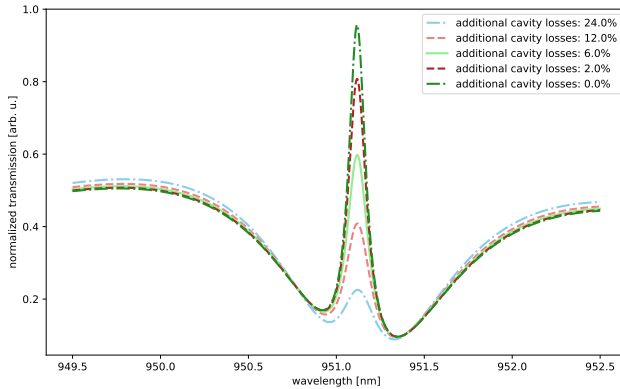


Figure 16: Resonant transmission spectra for different values of the additional loss term L , of a symmetric double Fano cavity of length $\sim 30\mu m$.

In this section we will investigate what happens when we introduce additional cavity losses⁴

$$L = 1 - |r_g|^2 - |t_g|^2, \quad (46)$$

leading to the modified condition

$$|r_g|^2 + |t_g|^2 + L = 1. \quad (47)$$

Figure 16 shows double Fano transmission spectra for a symmetric cavity with varying values for the additional cavity losses. It is readily seen that the maximum value reached in each spectrum is rapidly reduced with the introduction of these losses.

Since the linewidth is defined as the HWHM of the transmission profile, this will naturally vary as a function of additional cavity losses. This is depicted in figure 17a where the HWHM is shown for different values of L . Examples of intracavity spectra taken for different values of L are shown in figures 17b and 17c, along with their respective least squares fits to the general Fano model in eq. (33) and linewidths found as fitting parameters hereof.

⁴Not to be confused with the often used definition of cavity losses given as $L = 1 - |r|^2$ where anything not being reflected back into the cavity is considered to have a contribution to the losses.

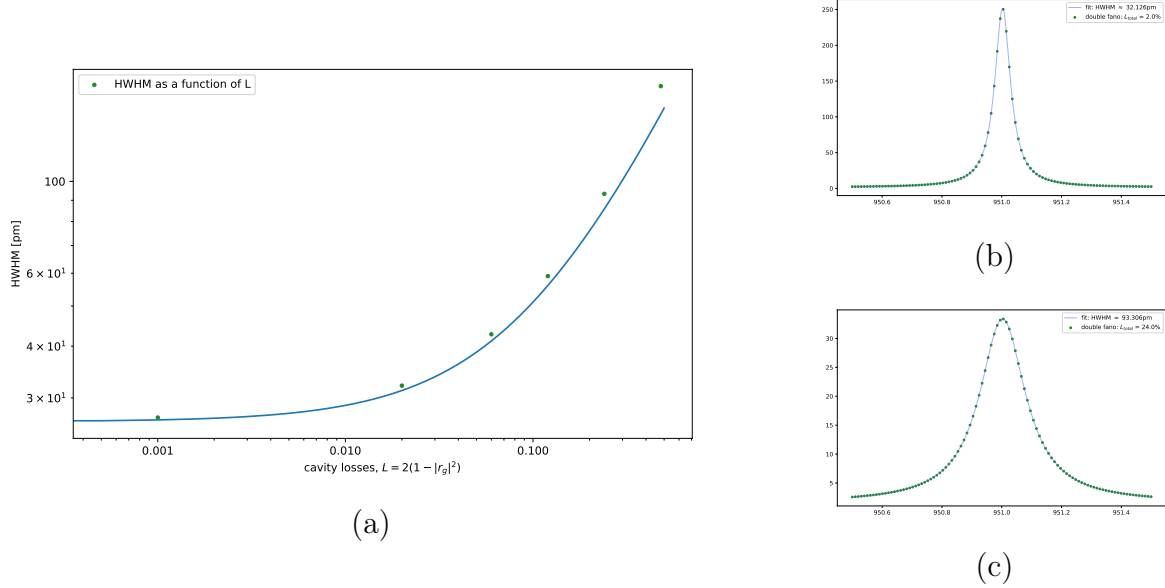


Figure 17: (a) shows the linewidth (HWHM) of a symmetric double Fano cavity of length $\sim 30\mu m$ as a function of additional cavity losses $L = 2(|r_g|^2 - |t_g|^2)$. Each point is found as a fitting parameter of a least squares fit of the intracavity double Fano spectrum for a certain value of L to the general Fano model. The plotted line indicates the analytical value of the linewidth (eq. 34) as a function of L , for comparison. In (b) and (c) are seen examples of intracavity double Fano spectra, with their respective linewidths, for cavities of $L = 2\%$ and $L = 24\%$, respectively.

Figure 17a shows the simulated linewidths of intracavity spectra as a function of total cavity losses L , and is compared with the analytical formula for the double Fano linewidth in eq. (39). It is seen that the analytical model proves, once again, to be a powerful predicting technique for the linewidth, and especially for cavities with relatively low losses.

2.4.5 Spectral detuning (lossless)

Up until this point, it has been assumed that the Fano mirrors making up the double Fano cavity has been identical, namely the cavity has been *symmetric*. However, in practice this is very unlikely to be the case, as any Fano mirror constructed is bound to have some uncertainties attached to the physical parameters describing it. For that reason we investigate the effect of an *assymmetric* cavity on the resulting transmission profile. Here we remember that each Fano mirror is described by a set of parameters, λ_0 , λ_1 , t_d , $\gamma\lambda$ and β , which respectively describe

the cavity resonance wavelength, guided-mode resonance wavelength, direct transmission, guided-mode resonance linewidth and additional losses of each grating. In order to model only a spectral detuning, we therefore simply change the parameters regarding the cavity and guided-mode resonance wavelengths, λ_0 and λ_1 by an amount corresponding to the detuning we wish to study. For this section the parameters will be given as

$$\begin{aligned} \lambda_0 &= 951\text{nm}, \quad \lambda_1 = 951\text{nm}, \quad t_d = 80\%, \\ \gamma\lambda &= 0.5\text{nm} \quad \text{and} \quad \beta = 10^{-6} \end{aligned} \quad (48)$$

for the unchanged Fano mirror, and

$$\begin{aligned} \lambda'_0 &= \lambda_0 + \Delta, \quad \lambda'_1 = \lambda_1 + \Delta, \quad t'_d = t_d, \\ \gamma\lambda' &= \gamma\lambda \quad \text{and} \quad \beta' = \beta \end{aligned} \quad (49)$$

for the *detuned* Fano mirror. Figure 18 shows the normalized reflectivity and transmission spectra of the Fano mirrors described by the parameters in eqs. (48) and (49).

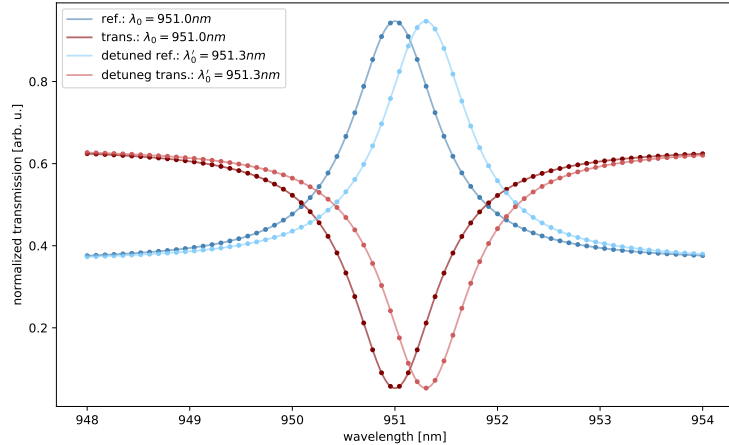


Figure 18: The normalized reflectivity and transmission spectra of the Fano mirrors described in eqs. (48) and (49) for detuning $\Delta = 0.3\text{nm}$.

As has been observed in previous sections, the Fano resonance transmission peak is present at the point where the grating reflectivity $r_g(\lambda)$ is maximized and transmission $t_g(\lambda)$ minimized. However, when $\lambda_0 \neq \lambda'_0$ and $\lambda_1 \neq \lambda'_1$, this is no longer a trivial conclusion to draw. The question of whether the cavity resonance should be tuned to match the guided-mode resonance wavelength of one grating or the other, or maybe somewhere in between does not have

an obvious answer. This will be further expanded upon later in section 2.4.6, but in order to move forward with the investigation of the spectral detuning we, for now, accept that the optimal cavity length, is the one corresponding to a cavity resonance λ_t given, exactly between the two guided-mode resonance wavelengths, as

$$\lambda_t = \frac{\lambda_{0,1} + \lambda'_{0,1}}{2}. \quad (50)$$

The subscript $0,1$ indicate that the two are interchangable, as the two are assumed identical at this time, and t is for *transmission* as this is, later on, to be used experimentally as the *transmission wavelength*.

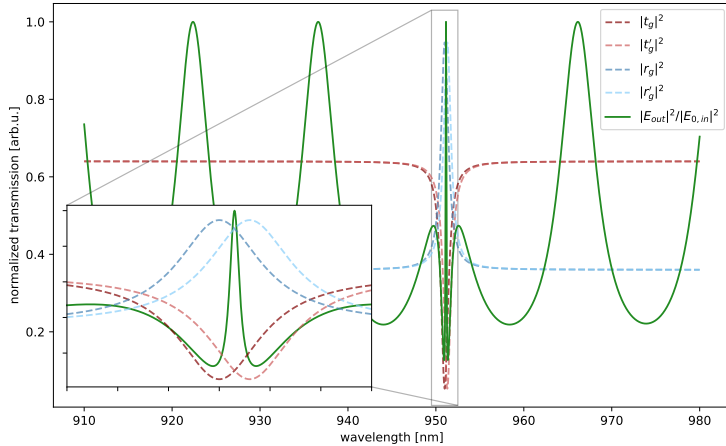


Figure 19: The double Fano transmission spectra of a cavity detuned by $\Delta = 0.3\text{nm}$, as seen in figure 18, together with the reflectivity and transmission spectra of the Fano mirrors used for the simulation.

Figure 19 shows the transmission spectrum of a detuned double Fano cavity with parameters corresponding to the transmission and reflectivity spectra in figure 18, meaning that $\Delta = 0.3\text{nm}$. The transmission wavelength λ_t is chosen such that eq. (50) is fulfilled, and correspondingly it is seen that the transmission peak is placed exactly between the maximum (minimum) reflectivities (transmissions) of the two grating, i.e. between the two guided-mode resonance wavelengths. Furthermore, it can be concluded that the detuning is chosen such that the overlap between the guided-mode resonances is still substancial enough for them to couple and hence for the the overall Fano resonance to be excited.

While knowing that a detuning of 0.3nm is acceptable in terms of exciting the Fano resonance in the lossless case is a nice result, it does not provide much in

terms of estimating the acceptable detuning for any experimental purposes. In figure 20a the double Fano transmission is shown for increasing detuning Δ and transmission wavelength $\lambda_t = (\lambda_{0,1} + \lambda'_{0,1})/2$.

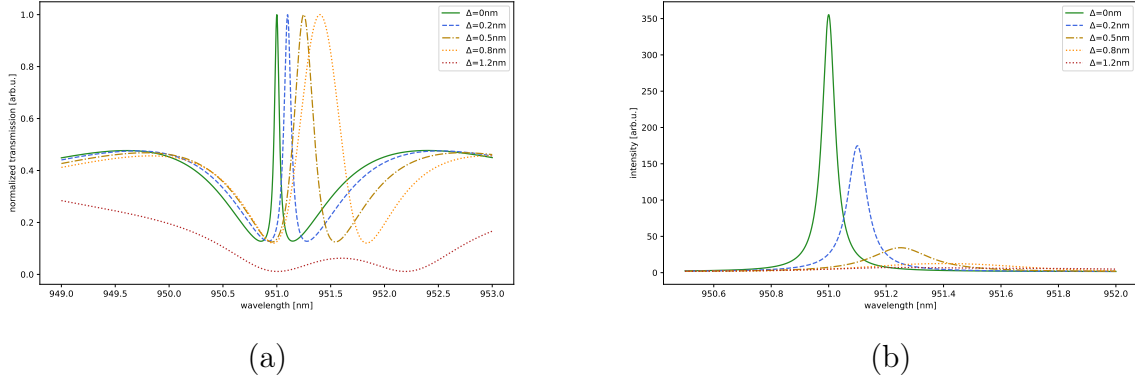


Figure 20: In (a) is seen lossless double Fano transmission spectra for increasing value of the detuning $\Delta = |\lambda_{0,1} - \lambda'_{0,1}|$. It is readily seen that the transmission wavelength $\lambda_t = (\lambda_{0,1} + \lambda'_{0,1})/2$ goes up, and that the linewidth likewise becomes larger with increasing detuning. The spectrum for $\Delta = 1.2\text{nm}$ shows the effect of the detuning becoming too large for the guided-modes of the two Fano mirrors to have substantial overlap and thus to sustain the Fano resonance. (b) shows the intracavity spectra corresponding to the transmission spectra in (a).

It is readily seen that with increasing positive detuning, relative to the resonant wavelength of the unchanged Fano mirror, the peak shifts to higher wavelengths, which in itself is trivial from eq. (50). The linewidth is also seen to increase with the detuning, and the peak eventually collapses when the overlap between the guided-mode resonance profiles of the two Fano mirrors becomes too small to sustain the Fano resonance. Figure 20b shows the intracavity spectra corresponding to the transmission spectra in figure 20a, and provides valuable insight into the mode density inside the cavity for the different values of Δ . It is clearly demonstrated by the two figures that the spectral overlap is a very crucial parameter of the double Fano cavity, and is paramount in describing the cavity's ability to sustain the Fano resonance modes.

2.4.6 Spacial detuning (lossless)

As mentioned above in section 2.4.5, any spectral detuning gives rise to the potential of a spacial detuning as $2l = m\lambda$ (eq. (??)) must be fulfilled for any sustained plane-wave mode inside a normal incident optical cavity. We denote the length corresponding to the resonance wavelength of the unchanged Fano

mirror as simply l , while the one for the detuned Fano mirror will be denoted as l' . Previously we assumed that the optimal length of a detuned double Fano cavity is the one where the so-called transmission wavelength is given as

$$\lambda_t = \frac{\lambda_{0,1} + \lambda'_{0,1}}{2}. \quad (51)$$

And while this does turn out to be the case, we must investigate the resonant length-dependence of the linewidth of the Fano resonance profile in order to arrive at this conclusion indefinitely.

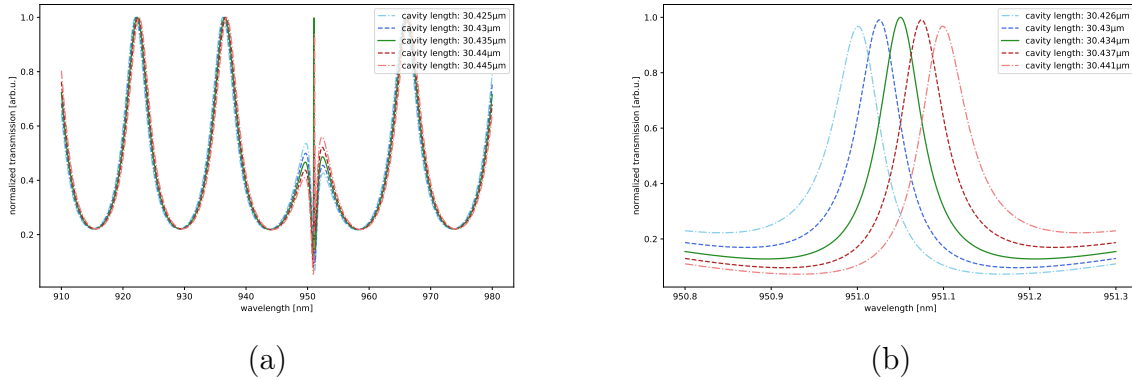


Figure 21: (a) shows lossless long-range transmission spectra of double Fano cavities of lengths $l \rightarrow l' \approx 30\mu m$ with $\Delta = 0.1nm$. (b) shows the same spectra as seen in (a), zoomed in on the range around the transmission wavelength λ_t .

Figure 21 shows double Fano resonance transmission profiles plotted for varying cavity length $l \rightarrow l'$ with detuning $\Delta = 0.1nm$. Looking at figure 21a we see the long range scan of the transmission profiles where there still appears to be a substantial overlap between the guided-modes of the two Fano mirrors. The main differences are seen as changes in the intensity in the immediate off-resonance regime. This is due to the dramatic wavelength (and thus length) dependence in the areas close to the resonance position, which makes even very small changes visible on the spectra.

Figure 21b shows the same spectra, but enhanced around the resonance wavelength, and this too shows that the substantial guided-mode overlap results in little visible change, except for shifting the peak position, when scanning between the resonant cavity lengths.

Figure 22 shows similar transmission profiles as in figure 21, only with an increased detuning of $\Delta = 0.3nm$. Looking at the long range scan in figure 22a

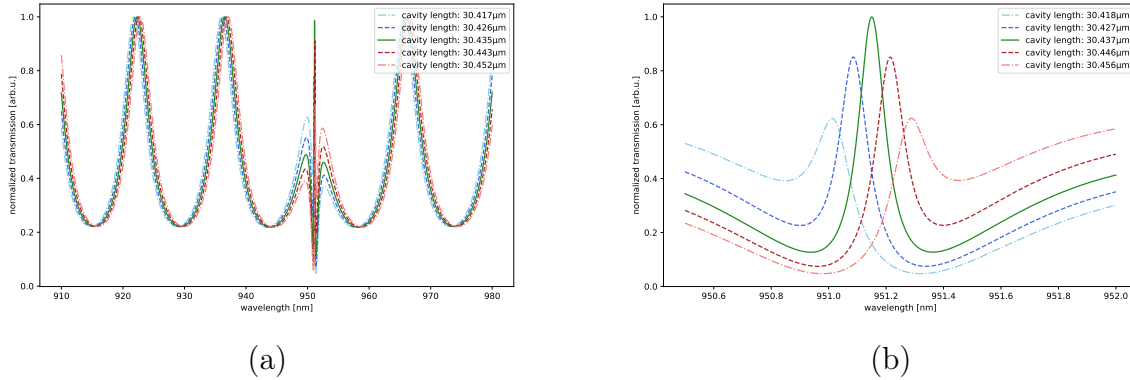


Figure 22: (a) shows lossless long-range transmission spectra of double Fano cavities of lengths $l \rightarrow l' \approx 30\mu\text{m}$ with $\Delta = 0.3\text{nm}$. (b) shows the same spectra as seen in (a), zoomed in on the range around the transmission wavelength λ_t .

and comparing with the one in figure 21a, it is seen that the displacement of the off-resonance Fabry-Perot like fringes have increased with the slightly higher detuning. This is not surprising as the Fabry-Perot cavity modes, like any other interference pattern inside a cavity must fulfill the brightness identity $2l = m\lambda$. Furthermore, the immediate off-resonance regime shows a slight increase in the intensity displacement when compared with the less detuned example.

Figure 22b, which shows the spectra enhanced around the resonance position, provides a more detailed image of what happens to the transmission profiles as a function of the cavity length. Here it is seen that the peaks at the edges of the length interval have varied in both position and height, much more dramatically than the ones in figure 21b. In short, the increased detuning has also increased the fractional length-dependence of the double Fano cavity⁵, as the resonance transmission profile seem to change *more* when varying the length of the cavity between the guided-mode resonance lengths, in this case.

Figure 23 shows the effect of a relatively large detuning of $\Delta = 0.8\text{nm}$. This is simply included for a visual representation of a detuning which is considered "too large" for any practical use. The long range scan in figure 23a shows that the Fabry-Perot like fringes are now too displaced to be compared in terms of their positions, and figure 23b showing the spectra enhanced around the resonance wavelength shows roughly the same trend as in figure 22b, only that this example is greatly broadened in comparison. It is though noted, that while

⁵It must be noted here that the range in which the cavity length is scanned is increased with the detuning. So the length-dependence is fractional in the sense that the step size is defined by the size of the interval.

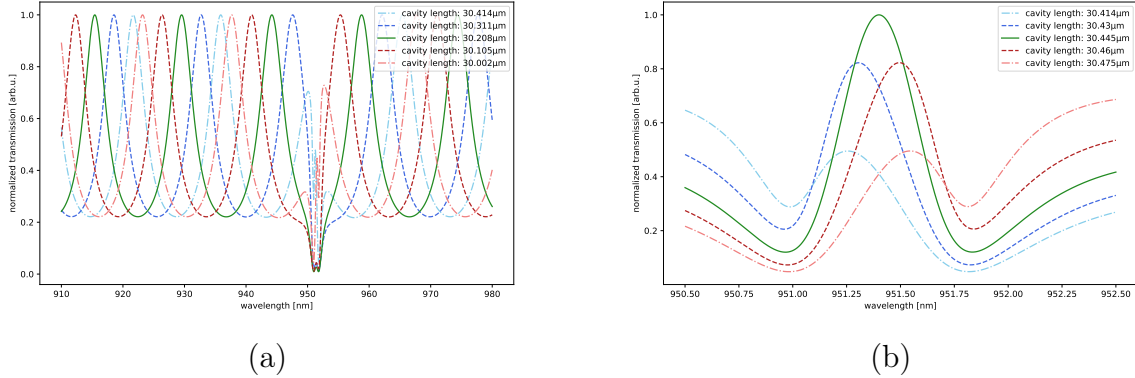


Figure 23: (a) shows lossless long-range transmission spectra of double Fano cavities of lengths $l \rightarrow l' \approx 30\mu\text{m}$ with $\Delta = 0.8\text{nm}$. (b) shows the same spectra as seen in (a), zoomed in on the range around the transmission wavelength λ_t .

broadened, the Fano resonance mode is sustained even for the relatively large detuning.

In order to get a clear and qualitative picture of the double Fano cavity transmission profile as a function of both cavity length and wavelength, we visualize the varying of both in a heat map and let the color indicate the transmission intensity. This is shown in figure 24a which depicts a lossless cavity of length $l \approx 20\mu\text{m}$ and detuning $\Delta = 0.3\text{nm}$. Here the movement of the resonance peak as a function of the cavity length is clearly seen as a slope of the "line" representing the high intensity region due to the Fano resonance.

Considering only the heat map, it is not easily visible which cavity length is the optimal one, however, the *magenta*, *cyan*, and *limegreen* lines across the heat map indicate slices which are depicted separately in figure 24b. It is seen by analysing the transmission profiles of these cavities of specific lengths, how they vary in both position and linewidth. The resonance wavelength positions are given relative to the cavity lengths chosen. The lengths and corresponding linewidths are given as

$$\begin{aligned} l_{magenta} &= 0.2l + 0.8l' \rightarrow HWHM_{magenta} = 71.3\text{pm} \\ l_{cyan} &= 0.8l + 0.2l' \rightarrow HWHM_{cyan} = 71.3\text{pm} \\ l_{lime} &= (l + l')/2 \rightarrow HWHM_{lime} = 58.6\text{pm}. \end{aligned} \quad (52)$$

It turns out that the linewidths of the cyan and magenta transmission profiles

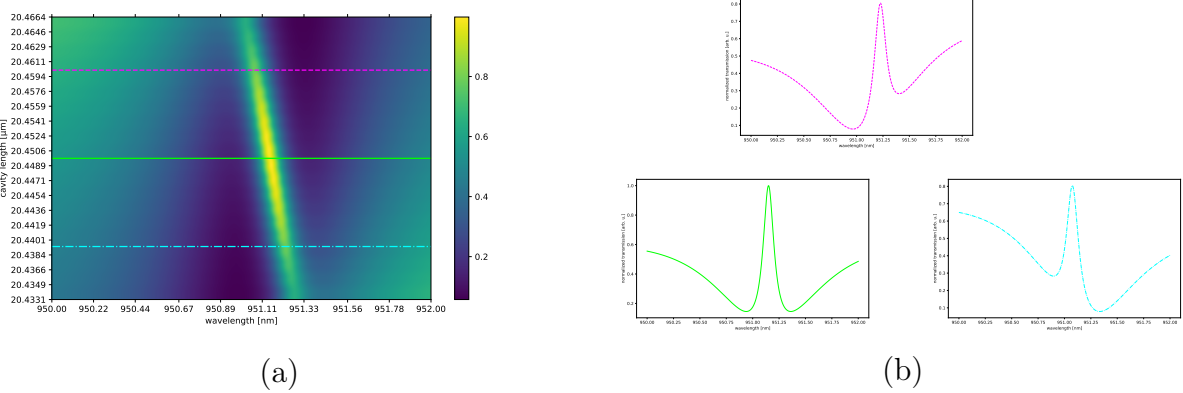


Figure 24: (a) shows a heat map of the lossless double Fano cavity transmission as a function of wavelength and cavity lengths ranging $l \rightarrow l' \approx 20\mu\text{m}$ for $\Delta = 0.3\text{nm}$. (b) show slices of the heat map for comparing different cavity lengths, and are indicated by their respective color and linetype in (a). The respective cavity lengths and linewidths are given as: $l_{\text{magenta}} = (0.2l + 0.8l')$, $HWHM_{\text{magenta}} = 71.3\text{pm}$, $l_{\text{cyan}} = (0.8l + 0.2l')$, $HWHM_{\text{cyan}} = 71.3\text{pm}$ and $l_{\text{lime}} = (l + l')/2$, $HWHM_{\text{lime}} = 58.6\text{pm}$.

are identical⁶, while the limegreen transmission profile seem to have a narrower profile at resonance.

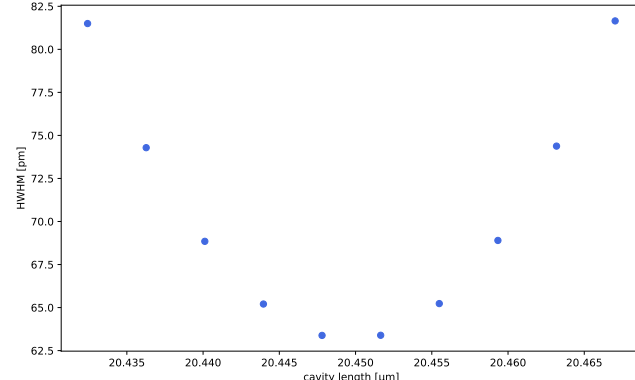


Figure 25: Linewidth as a function of cavity length $l \rightarrow l'$. Each point is found as a fitting parameter from a least squares fit of the intracavity lossless double Fano spectrum for each respective cavity length, to the generalized Fano model in eq. (33).

⁶This is only exactly correct because the only varied parameter of the two Fano mirrors are the cavity- and guided-mode-resonant wavelengths λ_0 and λ_1 . In a more realistic case where several parameters vary, the attributes of the transmission profiles are unlikely to act fully symmetrically when varying the length $l \rightarrow l'$.

This trend is further examined in figure 25 where the linewidths of intracavity spectra are shown as a function of the cavity length. The parameters used are the same as in figure 24 and clearly indicates that the optimal cavity length of a detuned double Fano cavity is the one fulfilling

$$\lambda_t = \frac{\lambda_{0,1} + \lambda'_{0,1}}{2}, \quad (53)$$

for the transmission wavelength λ_t , and thus corresponding cavity length l_t .

As a visual and qualitative representation of the effect of increasing the detuning Δ , figure 26 shows heat maps similar to the one in figure 24, but for a range of values for the detuning $\Delta = 0.1\text{nm} \rightarrow \Delta = 0.9\text{nm}$. It is readily seen that the aforementioned slope of the high intensity region, indicating the resonance peak, increases with the detuning. This is a representation of the peak moving to higher wavelengths, both for the optimal transmission wavelength and for the one closer to the detuned Fano mirror guided-mode resonance. The broadening of the peak is also displayed in a way that is, while only qualitative, convincing.

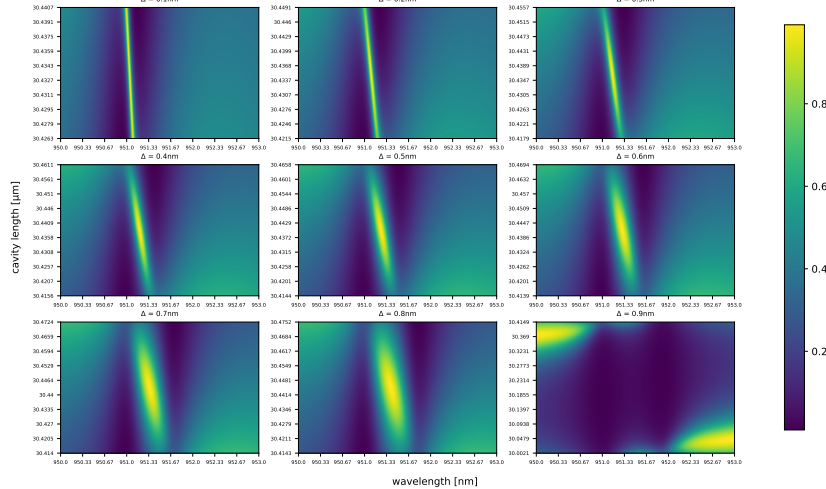


Figure 26: Series of heat maps showing lossless double Fano transmission spectra as a function of the cavity length, for increasing detuning Δ . The movement of the resonant wavelength is shown as the increasing slope of the high intensity region representing the resonance, for increasing detuning Δ . The broadening as a function of detuning is easily seen as it is qualitatively displayed in the series of figures until the spectral overlap makes the cavity unable of sustaining the Fano resonance.

The last image in figure 26, displays the case of $\Delta = 0.9nm$. Here it is seen that the spectral overlap has become too small to sustain the Fano resonance inside the cavity, and the intensity at the, previously, optimal transmission wavelength is therefore at a minimum. If however, we look at the areas of the heat map corresponding to cavity lengths of exactly l or l' and wavelengths $\lambda_{0,1}$ or $\lambda'_{0,1}$, we see that there is a slight increase in the transmission intensity. This is due to the fact that the cavity, in this position, corresponds to a single Fano cavity with a low finesse, as one of the Fano mirrors are exactly on resonance while the other is so far away that it acts as simply a poor "broadband" mirror.

3 Method

3.1 The experimental setup

The experimental setup used to optically characterize the Fano mirrors, single- and double Fano cavities is illustrated in figure ?? where the whole setup is sketched in figure 27 and the specific part of the setup surrounding the cavity, outlined by the dashed line in figure 27, is subsequently shown in figure 28a.

In order to effectively conduct the experiments in this project, it is imperative to be able to control certain parameters. Each element in the experimental setup is thoroughly considered for each their purpose in this regard, these will be outlined in this section.

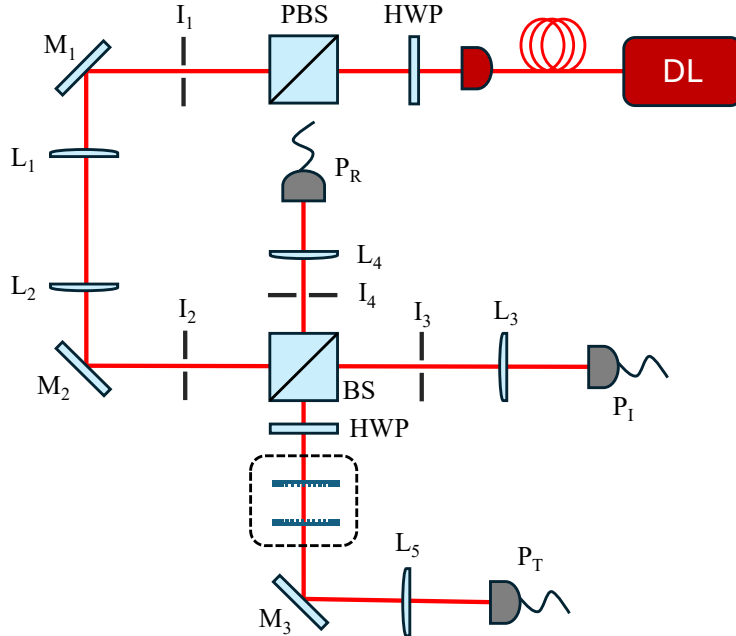


Figure 27: Schematics of the experimental setup for measuring Fano cavity transmission- and Fano mirror transmission/reflection spectra. The diode laser *DL* emits light into the setup through the optical fiber, the $\lambda/2$ -waveplate *HWP* and polarizing beam splitter *PBS* ensures the light is linearly polarized and the optical telescope consisting of lenses $L_{1,2}$ modifies the beam waist to fit the given purpose. Detectors $P_{T,R,I}$ records the transmitted, reflected and incident light, respectively and the second HWP makes it possible to tune the polarization of the light just before the light is incident on the Fano cavity/mirror. The dashed line indicates the cavity setup seen in detail in figure 28. I_{1-4} and M_{1-3} indicate apertures/iris' and mirrors, respectively.

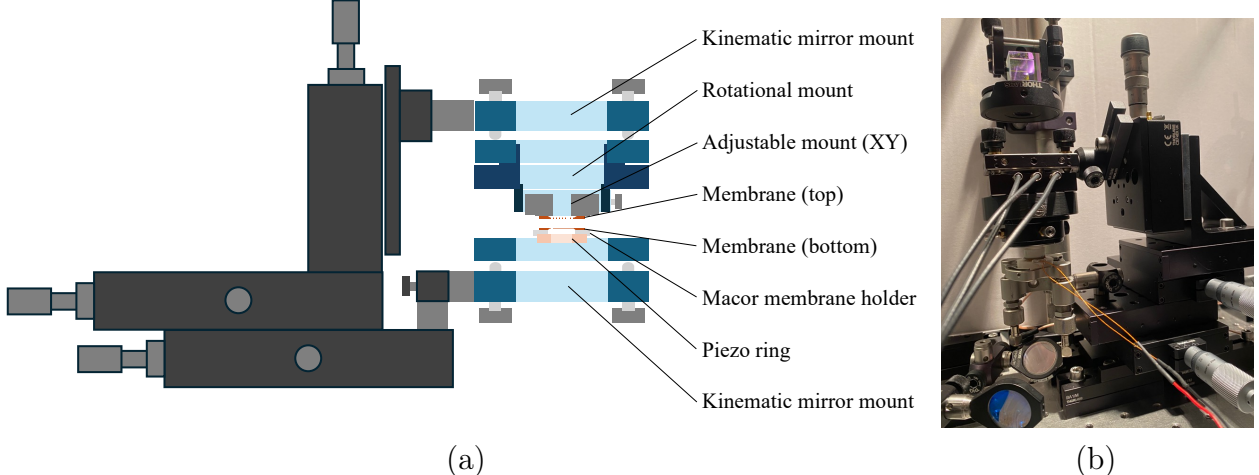


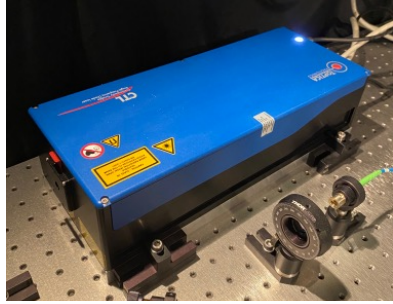
Figure 28: (a) shows a sketch of the schematics of the Fano cavity setup located inside the dashed line in figure 27. The stages attached to both the top and bottom of the cavity are used to spatially align the Fano mirrors of the cavity, while the kinematics mirrors are used to adjust for the angular degrees of freedom. The piezo ring is used to scan for and tune the optimal length of the cavity and the rotational and adjustable xy-mounts are used for aligning the top of the cavity, when the bottom is aligned with respect to the laser, and both are hence fixed. (b) shows a picture of the cavity setup depicted schematically in (a). Note that the setup, both in (a) and (b), depicted is the one used to measure double Fano cavity transmission, and would thus be modified for a Fano mirror characterization.

3.1.1 Tunable diode laser

As shown in figure 27 the laser source used for the optical characterizations is coupled into the setup through an optical fiber. The laser used is a *Toptica DLC Pro* tunable CW diode laser with a range for the transmission wavelength of 910 – 980nm. The laser and controller are both depicted in figure 29. The optical fiber is a *P3-780PM-FC-10* fiber from Thorlabs which is a single mode⁷ polarization-maintaining optical fiber with an effective range of 770 – 1100nm. Between the Toptica laser and the incoupling end of the fiber, a $\lambda/2$ -plate (HWP) and *polarizing beam splitter* (PBS) is placed in order to be able to control the incident power of the laser and to only couple linearly polarized light into the setup.

The light being emitted from the optical fiber is sent through another HWP

⁷A single mode fiber can only sustain the TEM00 mode, which means that the output is known to be perfectly Gaussian.



(a)



(b)

Figure 29: The Toptica DLC Pro tunable CW diode laser (a) and the controller (b) used to tune the wavelength of the output beam.

and PBS in order to be able to control the resulting polarization in the setup even more precisely, should there be any discrepancies of the light coupled into the fiber. The out-coupling fiber with the HWP and PBS is shown in figure 30.

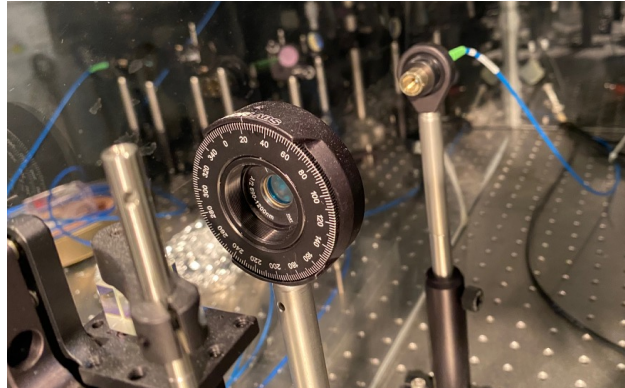


Figure 30: The out-coupling end of the P3-780PM-FC-10 polarization maintaining optical fiber from Thorlabs along with the HWP and PBS ensuring linear polarized light incident on the cavity or Fano mirror.

3.1.2 $\lambda/2$ - waveplate

A $\lambda/2$ -waveplate, or HWP, is constructed of a so-called bi-refringent material (most commonly crystalline quartz), which means that it has slightly different refractive indices for incident light of different polarization axis'. Generally a HWP will have a *fast-* and *slow axis*, where it is understood that light polarized along the fast axis experiences a lower refractive index (and hence moves faster), than that along the slow axis. In this way the HWP separates the components of unpolarized light that has perpendicular and parallel polarizations with respect to the fast axis.

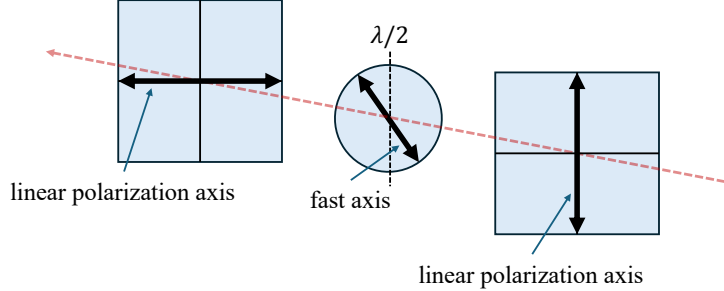


Figure 31: A simple sketch of the effect of a HWP on linearly polarized light.

The effect of the HWP on linearly polarized light, is an effective rotation of the polarization axis, this is sketched simply in figure 31. It can be shown that the polarization axis is rotated according to the angle between the fast axis of the HWP and the incident polarization axis. A relative angle θ will thus result in a rotation of 2θ , e.g. if $\theta = 45^\circ$, this will constitute a rotation from completely p-polarized light to completely s-polarized light. This is the specific scenario sketched in figure 31[14]. In this way a rotating HWP can allow one to alter an incident linearly polarized beam to be polarized along any axis, and is thus a necessary component for this particular setup.

3.1.3 Optical telescope

The linearly polarized light transmitted through the PBS passes through plano-convex lenses of positive focal lengths f and f' , L_1 and L_2 , which together makes up an optical telescope used to manipulate the beam waist w_0 incident on the cavity or Fano mirror.

Figure 32a shows schematics of the general way an optical telescope is utilized to manipulate the beam waist of a laser beam.

When the incident beam hits L_1 it is focused according to its focal length f , and by inserting another lens L_2 of a relatively longer focal length one can *catch* the beam at the desired beam waist. If the focal length f' of L_2 is sufficiently long, compared to the path of the beam after the lenses, the beam will be approximately collimated and remain at the waist obtained when incident on L_2 .

3.1.4 Transmission, reflection and incident photo-detectors

After passing the optical telescope the beam reaches a simple 50/50 beam splitter (BS) which transmits 50% of the light while reflecting another 50%. The

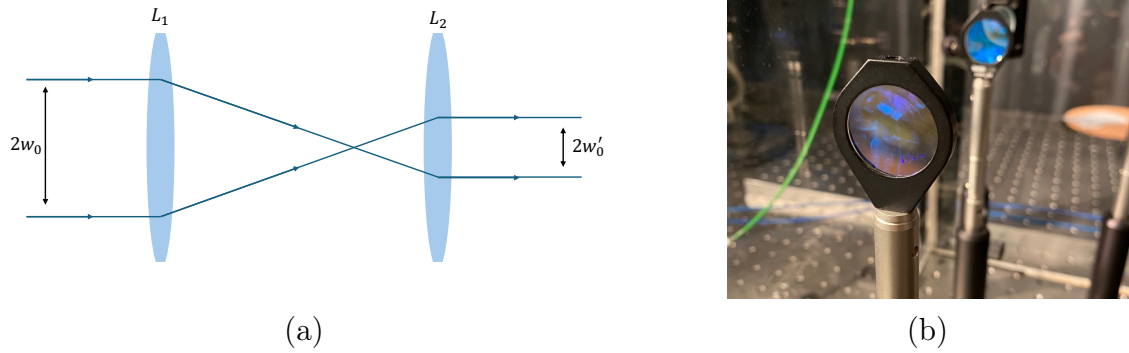


Figure 32: (a) shows simple schematics of an optical telescope used to alter the waist of an incoming collimated beam, while (b) shows a picture taken of the actual optical telescope used in the setup.

reflected light is then incident on the cavity or Fano mirror (target).

The transmitted light passes through a lens L_3 , which is focused on a photodetector P_I used for reference measurements and later normalization. Since the tunable laser in nature varies in power with the wavelength, it is necessary to keep track of these fluctuations and correct for them in data analysis.

The transmitted light is sent through, yet another, HWP which in this case is used only to alter the polarization of the light incident on the target. After the beam, or a portion of it, has passed the target it is sent through a lens L_5 focused onto the transmission detector P_T .

The part of the light incident on the target that is *not* transmitted, is reflected back onto the BS which then transmits 50% once again, and thus reflects the other 50%. The transmitted part here is focused through the lens L_4 onto the reflection detector P_R .

3.1.5 The double Fano cavity measurement setup

The cavity measurement setup shown in figure 28a is the one used to measure the transmission spectrum of a double Fano cavity consisting of two Fano mirrors. This part of the setup consists of two sets of standard $PT1 \mu\text{m}$ -stages from Thorlabs combined to provide precise movement of each Fano mirror in the xy-plane.

Examining the structure from the bottom (as it is built), a kinematic mirror mount is attached to the lower set of xy-stages, this is used to control the angular degrees of freedom of the Fano mirror which makes up the bottom of the cavity.

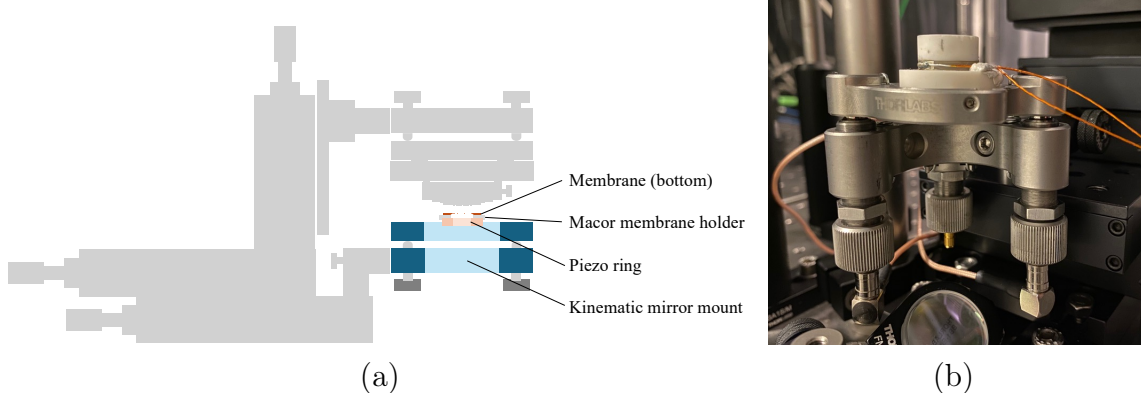


Figure 33: (b) shows a picture taken of the *bottom* part of the double Fano cavity setup, while (a) depicts the corresponding schematics.

On the mirror mount, a *NAC2123* piezo ring actuator from Noliac is firmly attached and connected to a piezo driver. The driver is capable of applying a fixed current, and thus manually controlling the piezo expansion, but is also connected to a frequency generator. The signal from the frequency generator can be used to modulate the piezo expansion by an alternating current, which practically scans the cavity length in a range according to the effective free stroke of the piezo ring⁸. Lastly, in order to be able to place the Fano mirror on the piezo ring, a ceramic Macor membrane holder is used. The bottom part of the cavity setup is highlighted in figure 33a.

The part of the setup built to control the Fano mirror making up the top of the cavity is slightly more complicated, as this is the Fano mirror that is, for practical reasons, aligned last. This means that additional degrees of freedom must be controlled by movement of the Fano mirror itself. The alignment procedure will be explained in detail in sections 3.2 and 3.3.

The top part of the cavity setup is attached to the second set of xy-stages and additionally to an *NFL5DP20* stage from Thorlabs in the z-direction in order to be able to change the length of the cavity. As for the bottom part of the cavity setup, a kinematic mirror mount acts as the base of the construction. This is, once again, to control the angular degrees of freedom of the corresponding Fano mirror. This mirror mount is equipped with piezo elements to control the angular degrees of freedom, by applied voltage, with higher resolution than for

⁸The NAC2123 piezo ring has an outer/inner diameter of 12mm/6mm and a height of 2mm. Its listed free stroke is $3.3\mu m$, which practically is likely slightly limited in the configuration used. To obtain the precise free stroke one can simply count the number of fringes resolved during one period as the length-dependent FSR is known to be $\lambda/2$.

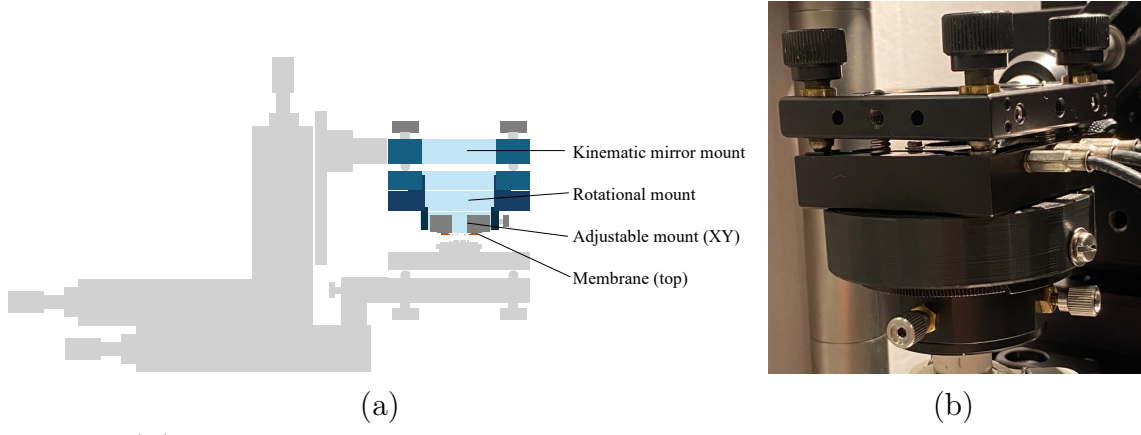


Figure 34: (b) shows a picture taken of the *top* part of the double Fano cavity setup, while (a) depicts the corresponding schematics.

the manual adjustments. On the mirror mount, a standard rotational mount with a 1 inch inner winding is attached in order to be able to control the rotational degree of freedom of the Fano mirror. An additional xy-adjustable mount is then used in order to effectively place the Fano mirror in the center of the rotational mount to ensure the rotational axis is in the center of the membrane. Finally, the Fano mirror is taped to a costume mount created to fit into the xy-adjustable mount. The top part of the cavity setup is highlighted in figure 34a, and presented separate from the setup to show how the Fano mirror is attached in figure 35.

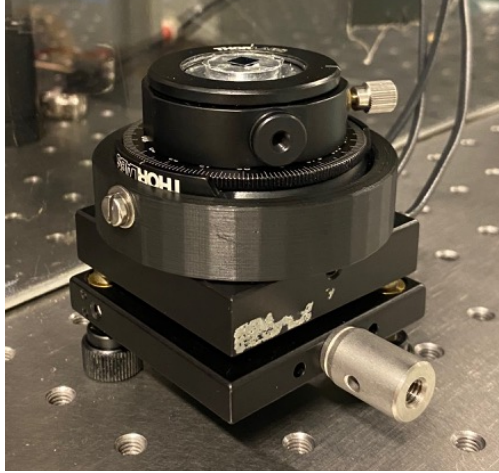


Figure 35: The top part of the cavity setup separated from the rest and flipped. Note that the Fano mirror attached with the tape is shown. The three wires visible are then ones that connect the piezo elements with a driver.

What has been outlined here is the setup utilized to optically characterize the double Fano cavity. If one wishes to do so for the single Fano cavity instead,

the setup would be modified such that the top part of the setup, highlighted in figure 34a, would only consist of the kinematic mirror mount. Inside the mirror mount would then be placed a broadband mirror. The rotational- and xy-adjustable mounts would here be redundant due to the rotational symmetry of any standard broadband mirror.

3.1.6 Acoustic noise reduction

When the cavity measurements were conducted it was apparent that the double Fano cavity was particularly prone to noise. While noise is not a very precise definition in its own, it did seem that the most prominent source was associated with the length of the cavity l . When applying a constant voltage to the piezo element depicted in figure 33, in order to achieve the correct length for sustaining the Fano resonance, the level started to fluctuate dramatically when approaching the resonance.

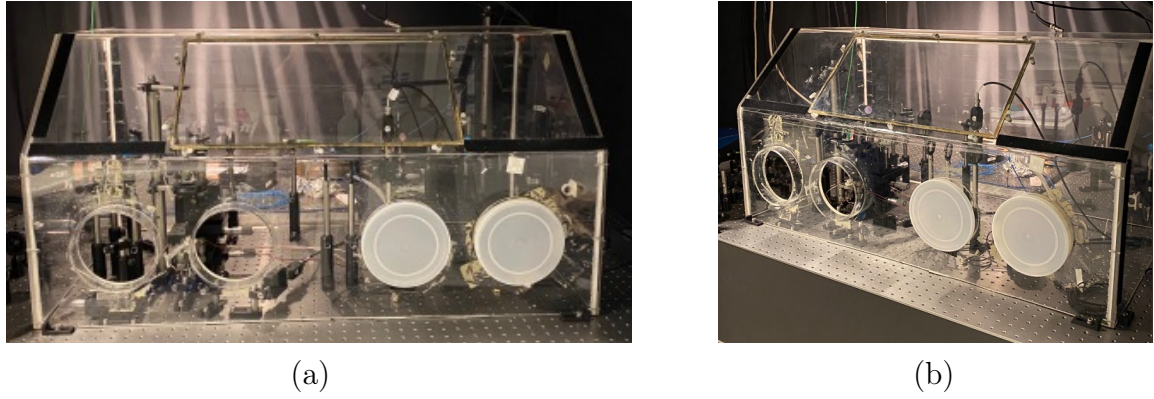


Figure 36: Front- (a) and side (b) views of the plexi-glass box used to reduce the acoustic noise in the setup.

By examining the characteristics of the noise when apparent, the source appeared to be acoustic in origin, i.e. making a sudden sound in close vicinity of the setup caused a spike in the noise level.

In order to reduce the acoustic noise, a plexi-glas box was placed around the entire setup as seen in figure 36. This proved to reduce the noise, and this improve the signal-to-noise, ratio substantially.

3.1.7 Additional equipment used

In order to record a measurement of any kind in the setup, a *Keysight Infini-iVision DSOX2024A* oscilloscope was connected with all the detectors P_T , P_R

and P_I in the setup. The oscilloscope, along with the Toptica laser, was then controlled by a Matlab script implemented by previous students/researchers of the lab.

Scanning the piezo element, by application of an alternating current also required additional equipment, and more specifically a frequency generator capable of generating a triangular signal with an offset. The frequency generator used was a *Keysight 33500B Waveform Generator*. Insight on scanning the cavity length using the piezo will be provided in section 3.3. The oscilloscope and frequency generator are shown in figure 37.



Figure 37: Pictures of the oscilloscope (a) and frequency generator (b) used during experimental investigations in this project.

3.2 Characterization of sub-wavelength grating

The sub-wavelength gratings, or Fano mirrors, used are commercially available high-quality silicone nitride *SiN* membranes suspended on a *Si* frame, which have been patterned into a grating. Figure 38a shows a packaged membrane from Norcada, which is the company who has provided all gratings/membranes used in this project. Figure 38b is a close-up picture of a bare membrane which have not yet been patterned, and includes a scale to provide perspective regarding the physical dimensions.

The patterned area of the Fano mirrors used throughout this project is $400 \times 400\mu m$, and this along with detailed dimensions of the whole membrane is sketched in figure 39.

3.2.1 The alignment procedure

In order to align the Fano mirror for its optical characterization only, the setup utilized is a simplified one, compared with the double Fano cavity setup shown

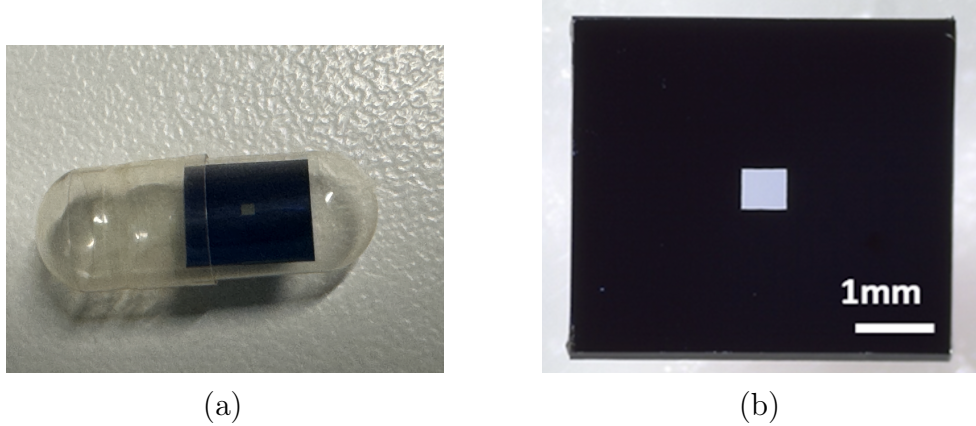


Figure 38: (a) shows an image of a packaged bare membrane, which has not yet been patterned, from Norcada. (b) is a close-up image of a bare membrane like the one in figure 38a.

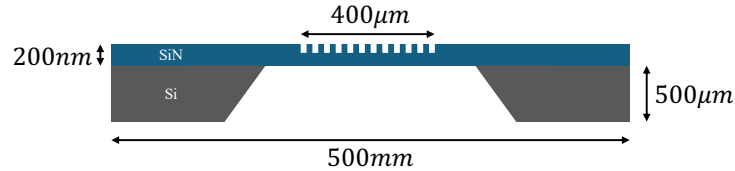


Figure 39: A simple sketch of the profile of a patterned membrane, i.e. a Fano mirror. It is seen that the width of the patterned area is $400\mu m$.

in figure 28a. This setup corresponds to one where only the *bottom* part is included, i.e. corresponding to the one highlighted in figure 33a. It must here be noted, that if the purpose of the Fano mirror alignment is to create a cavity, the top part shown in figure 34a must of course be utilized as well.

The goal of the alignment procedure is to ensure that the coupling between the guided-mode and the mode of the laser is maximized, this is outlined in section 2.2. The transmission of the Fano mirror is measured during alignment with a *PM100D* digital handheld optical power meter from Thorlabs, and progression of the alignment procedure is understood as minimizing the transmission. The behavior of the Fano mirror transmission, when perfectly aligned, can be seen in figure 8, where it has been simulated for a Fano mirror of arbitrary parameters. When aligned, the guided-mode resonance wavelength can thus be found. This is practically done by scanning the expected wavelength range using the Toptica laser and recording the wavelength at which the transmission is minimized.

The three degrees of freedom, in which the alignment of the Fano mirror is optimized, are the spacial coordinates (x, y), the rotational degree of freedom,

and the two angular degrees of freedom. It is assumed at this point that the waist of the beam incident on the Fano mirror is optimal, this will be expanded upon in section 3.2.2.

The general order in which the alignment is done is given as:

1. xy-plane alignment.
2. Alignment of the angular degrees of freedom (adjusting the kinematic mirror mount).
3. Rotational alignment (adjusting the HWP placed prior to the cavity setup).

xy-plane alignment

The spacial alignment of the Fano mirror in the xy-plane is simply done by movement of the xy-stages (linear μm -stages from Thorlabs) shown in figure 28a. Here it is crucial to know how the transmission level behaves qualitatively as a function of the xy-positions when the wavelength of the laser is off-resonance with respect to the guided-mode of the Fano mirror. Due to the effective thickness of the membrane in patterned and un-patterned areas being different, the transmission properties will vary slightly. This can be utilized in order to align these parameters effectively. Assuming one of the coordinates, x or y , is optimal, and one scans across the other as indicated in figure 40, it will be evident that the transmission is constant when the entire beam is incident on the bare membrane, while it will experience a slight decrease in the patterned area, simply due to the lower effective thickness of the structure in this area. For this reason the optimal alignment in this direction is found as the minimum transmission as a function hereof.

Angular alignment

Adjusting the angular alignment, which is done by adjusting the screws on the kinematic mirror mount holding the piezo ring and the Macor membrane holder, is crucial for the evaluation of the guided-mode resonance wavelength. As reported by Parthenopoulos et al. in [7] the resonance wavelength of the guided-mode depends strongly on the angle of incidence.

In figure 27 the components I_{1-4} indicate apertures (iris') used for the angular alignment. Specifically I_1 and I_2 are used to track the back-reflection of the

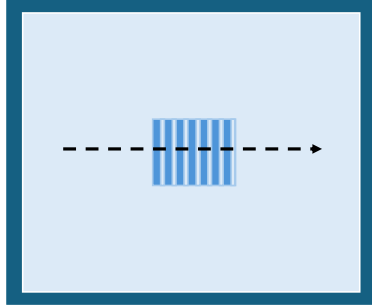


Figure 40: Simple sketch of a patterned membrane, i.e. a Fano mirror. The darker area surrounding the *SiN* membrane is the *Si* frame and the dark blue lines in the center indicate the $400 \times 400\mu m$ patterned area. The black dotted arrow is indicative of scanning across the membrane, by moving it relative to the beam, using one of the linear stages.

beam incident on the Fano mirror to ensure a high degree of overlap as possible. A complete overlap indicates that the incident beam is normal to the Fano mirror surface.

Rotational alignment

The Fano mirrors provided by Norcada are of so-called TM polarization, meaning that the magnetic field is parallel to the grating lines, and is thus perpendicular to the electric field. Since the polarization is defined along the axis of the electric field, this means that the polarization axis must also be perpendicular to the grating lines, as this ensures the interaction is maximized[15].

For this reason the rotational alignment is vital to achieving the correct minimum transmission wavelength of the Fano mirror.

Since no rotaitonal degree of freedom is appointed the Fano mirror itself, and that this would greatly complicate the alignment procedure, the rotational alignment is achieved by changing the polarization of the incident light. This done by adjusting hte rotating HWP placed immediately before the light hits the Fano mirror surface and is possible due to its effect on linearly polarized light illustrated in figure 31.

3.2.2 Adjusting and measuring the beam waist

In section 3.2.1 we assumed an optimal beam waist as the alignment procedure was outlined. This was due to the fact that the beam waist optimization is unnecessary unless the entire setup is rebuilt or if the size of the Fano mirror

is changed. Since the patterned area of the Fano mirrors characterized in this project was only $400 \times 400\mu m$, the beam waist optimization was only done once.

As is evident from figure 32a how an optical telescope was utilized to tune the waist size w_0 of the collimated laser beam. In order to determine the optimal value of w_0 the second lens L_2 was moved back and forth without diverging from the position where the optical axis passed through the center of the lens. The minimum transmission was recorded for each iteration, and the transmission would converge towards its minimum value (or at least the lowest achievable value). When the minimum transmission as a function of w_0 was found, this was measured using the *razor blade method*. The razor blade method is a simple tool to, fairly accurately, measure the beam waist of a Gaussian laser beam by *cutting* the beam gradually with a blade. The distance the blade moves is recorded along with the transmitted intensity, and the two are thus directly correlated[16].

An arbitrary Gaussian distribution, corresponding to a laser beam in the TEM00 mode, is shown on the left in figure 41, while the right plot shows the integral of the distribution as a function of the razor blade position, which corresponds to an error function.

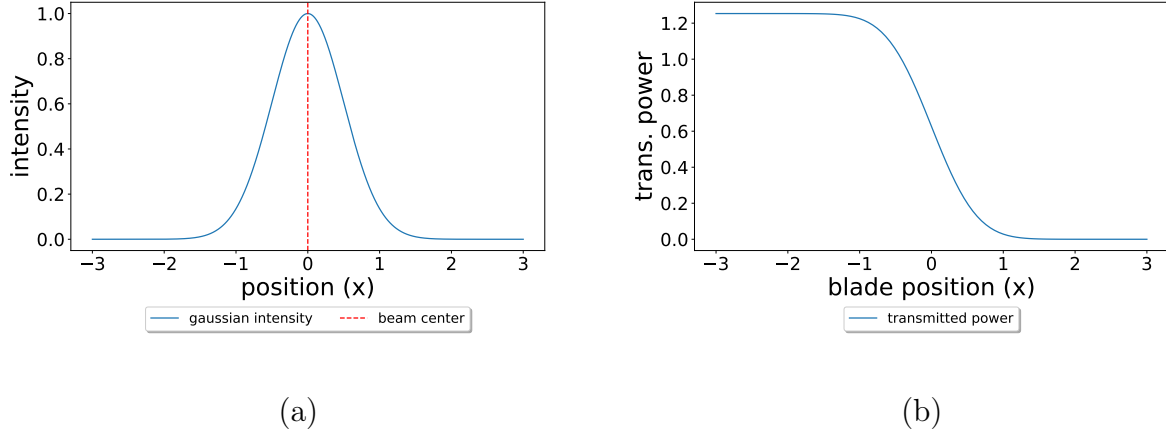


Figure 41: The left plot (a) shows an arbitrary Gaussian distribution, and the red dashed line indicate the placement of the maximum value. The right plot (b) shows the transmitted intensity as a function of the position of the razor blade, as the razor blade method is simulated, i.e. the beam is gradually covered with the blade.

In practice the blade position was recorded by counting the turns made on a

linear μm -stage with the razor blade attached, and the transmitted intensity was recorded live by a power meter from Thorlabs. The power of the laser beam without being *cut* by the blade was tuned to $\sim 1\text{mW}$ such that the percentile change was intuitively seen. The linewidth of the Gaussian beam is then approximately given as the distance between the two cut-off points where the transmitted intensity is given as 16% and 84%⁹. The optimal value for the linewidth was found to be

$$\delta\lambda_{400\mu\text{m}} \approx 160\mu\text{m}. \quad (54)$$

3.2.3 Obtaining normalized transmission/reflection spectra

When the Fano mirror and the surrounding setup is completely aligned, it is time for the optical characterization. In order to do so, a series of measurements is necessary to obtain normalized transmission and reflection spectra which rightfully represent the optical properties of the Fano mirror.

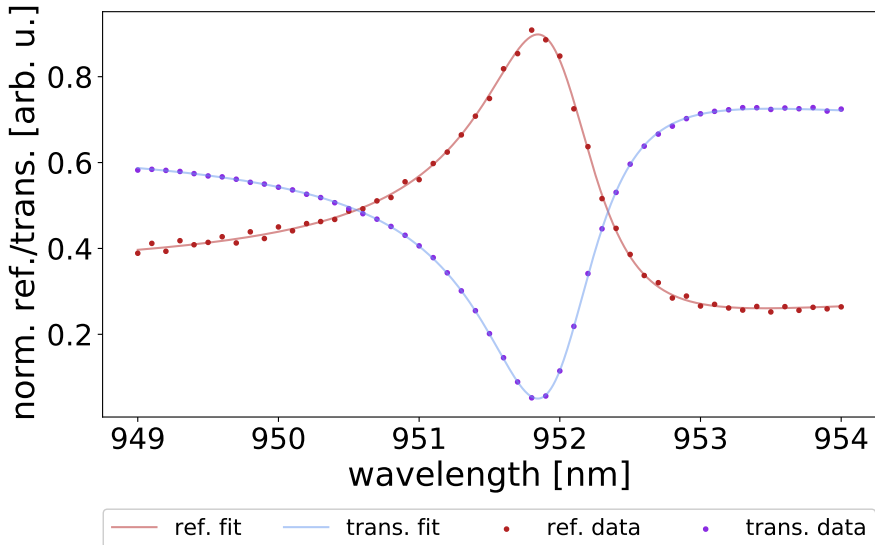


Figure 42: Normalized transmission and reflection spectra of $400 \times 400\mu\text{m}$ Fano mirror *G1*.

The structure of such measurements is given as follows:

⁹In reality this interval corresponds to the width according to two standard deviations 2σ , which is only approximately equal to the linewidth.

1. The transmission and reflection intensities as a function of wavelength are measured using the reflection detector P_R and the transmission detector P_T , while the signal measured in detector P_I is recorded as a reference measurement. The positions of all detectors are shown in figure 27.
2. The Fano mirror is removed and identical measurements are done for an "empty" setup. The purpose of this measurement is to measure the signal when *all* the incident light is transmitted, and *no* light is reflected. This data is used to normalize the transmission intensities obtained in the first measurement.
3. On the former position of the Fano mirror, a highly reflective (HR) mirror is now placed, and all measurements are repeated. This is corresponding to *all* the incident light being reflected, and *no* light being transmitted. This data is used to normalize the reflection intensities obtained in the first measurement.
4. Lastly, a measurement of the background signal is taken, by simply blocking the laser before it enters the setup and repeating the measurements.

The normalized values are then given as

$$T_{norm} = \frac{(T - bg)/(T_I - bg)}{(T' - bg)/(T'_I - bg)} \quad (55)$$

for the transmission amplitudes, and

$$R_{norm} = \frac{(R - bg)/(R_I - bg)}{(R' - bg)/(R'_I - bg)} \quad (56)$$

for the reflection amplitudes. Here $T = |t|^2$ and $R = |r|^2$ denote the transmission and reflection amplitudes measured by P_T and P_R in step (1), T' and R' are the values measured for the transmission- and reflection amplitudes in steps (2) and (3), respectively, and the subscript I indicates values obtained by the incident detector P_I for its corresponding measurement type. The background values obtained in step (4) are subtracted, these are labeled bg . Figure 42 shows an example of normalized spectra obtained by measurements (1)-(4) and calculations of eqs. (55) and (56).

3.3 Cavity measurements

The cavity measurements here, primarily, outlined will be that of the double Fano cavity. The single Fano cavity measurement procedure will secondarily be

clear as a simplification of the one for the double Fano cavity.

Very simply put for the cavity measurement procedure, is that one must go through the Fano mirror alignment process outlined in section 3.2 twice. One time for the bottom of the cavity, and then once for the top of the cavity, whereafter the two Fano mirrors are broad together according to the wanted cavity length and the transmission is recorded. However, this procedure contains many degrees of freedom and practicalities making it difficult to simply align each Fano mirror independently of each other. This section will go through each step of the process of arriving at a meaningful measurement of the transmission of the double Fano cavity. The reflections of improving the used method will be included in the discussion section.

3.3.1 Aligning the double Fano cavity

Before considering beginning to align the double Fano cavity, it is imperative to have two Fano mirrors which have similar physical dimensions, and thus be described by similar parameters as presented in section 2.2. In order to find a *match*, the only valid method is to use brute force and simply characterize Fano mirrors until a match is found. The batch of tested Fano mirrors in this project all came from the same order delivered by Norcada, as this was assumed to provide the best chances for a match. The condition for the spectral detuning $\Delta = |\lambda_{0,1} - \lambda'_{0,1}|$ of otherwise identical and lossless Fano mirrors is outlined in section 2.4.5.

Assuming a match is found, which we denote G_1 and G_2 ¹⁰, the alignment process is given as follows:

1. The bottom, i.e. the arbitrary Fano mirror G_1 , of the cavity is aligned according to the procedure outlined in section 3.2. This means that the incident beam is centered on and normal¹¹ to G_1 , and the polarization of the light is aligned such that the electric field is perpendicular to the grating lines. The wavelength of the laser is scanned, and the one corresponding to the guided-mode resonance of G_1 is recorded.
2. The bottom grating position is marked and the macor membrane holder

¹⁰ G here stands for *grating* while 1, 2 is indicative of the distinction between the two arbitrary Fano mirrors.

¹¹A trick to determine the degree of accuracy of the angular alignment is to periodically block the light reflected from the Fano mirror, and thus make this flicker. This way the flickering light is easily distinguishable from the incoming light and by examining the light at apertures I_2 and I_1 from all sides perpendicular to the propagation direction, the needed angular adjustments become clear.

(the macor membrane holder can be seen in figure 28a) containing G_1 is removed and stored safely. Now the laser polarization and spacial coordinates of G_1 are fixed and must not be changed in the following steps of the alignment procedure. The marks used to indicate the position of G_1 is shown in figure 43.

3. The top part of the cavity is inserted, but *without* the other Fano mirror G_2 in place, as the kinetic mirror- and rotational mounts first need to be centered in the beam. This is done by inserting a $100\mu m$ pinhole, specifically designed for the purpose, into the rotational mount. The spacial and angular coordinates of the top mount is thus changed to maximize the signal through the pinhole. The centering is then tested by rotating the pinhole and ensuring that the signal does not change, i.e. that the center of the rotational mount does not move out of the beam by rotating it. When this is satisfied, the top mount is removed and the spacial coordinates are considered aligned and thus fixed. The so-called *pinhole alignment method* will be explained in greater detail in section 3.3.5.
4. The Fano mirror G_2 is placed, with tape, onto the xy-adjustable mount (see figure 28a), which is then fastened to the rotational mount. The top mount now completely resembles the one shown in figure 35. G_2 is now aligned following a similar structure as the one outlined in section 3.2, but with the constraint of the above parameters being fixed. G_2 is moved into a position where it is centered with respect to the incident beam by adjusting the xy-adjustable mount, and the Fano mirror itself is now rotated to match the polarization of the laser. The angular alignment is done very similarly to that of G_1 , as the kinetic mirror mount is here used. When G_2 is aligned, the wavelength is once again scanned, and the one matching the guided-mode of G_2 is recorded.
5. The top mount, including G_2 , is now removed from the setup and all degrees of freedom are expected to be aligned. The trick to make sure that the angular alignment is preserved when re-inserting the top mount is that the back reflection is centered in the aperture I_4 depicted in figure 27, this way one can quite easily regain the approximate angular alignment.
6. The macor mebrane holder, with G_1 placed on it, is now re-inserted into the bottom of the setup and the Toptica laser is set to the guided-mode resonance wavelength according to G_1 . In this way G_1 is carefully placed

according to the marked position (see figure 43) and adjusted, by hand, to achieve the same minimum transmission as before it was removed.

7. The top mount, including G_2 , is now too re-inserted, and adjusted by hand such that the back-reflected beam overlaps with the aperture I_4 .
8. The wavelength of the Toptica laser is now set to the transmission wavelength given in eq. (50), the wavelength exactly between the guided-mode resonance wavelengths of G_1 and G_2 , i.e. $\lambda_t = (\lambda_{0,G_1} + \lambda_{0,G_2})/2$.

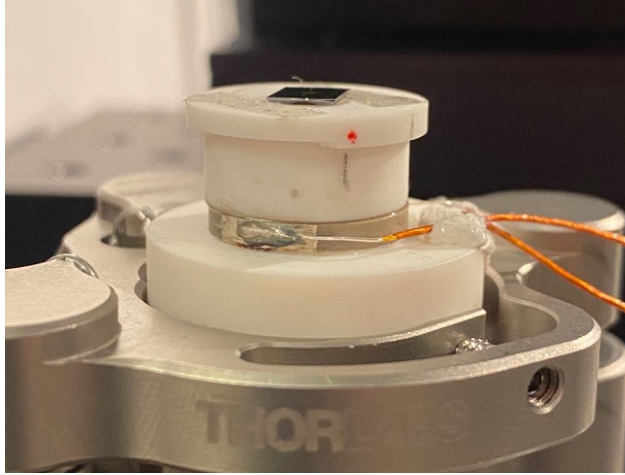


Figure 43: A close-up of the bottom part of the cavity with a Fano mirror placed on the macor membrane holder. Note the marks used to re-insert the bottom part of the cavity as mentioned in steps 2 and 6.

3.3.2 Cavity resonance - the piezo ring

Once the double Fano cavity is successfully aligned with respect to the individual guided-modes of G_1 and G_2 , the cavity mode (i.e. the cavity length) must be made to coincide in order to excite the Fano resonance mode. Here we remember that the cavity length is related to the cavity mode through the general Fabry-Perot cavity brightness condition $2l = m\lambda$.

In order to tune the cavity length on the scale necessary, it is scanned by periodically varying the length of the cavity using the piezo ring and applying an alternating current specified with the frequency generator shown in figure 37b. In this way the resulting signal recorded with photo detector P_T and seen in the oscilloscope shown in figure 37a is time-dependent and seen as fringes. Figure 44 shows the corresponding fringes for an approximate cavity length of $100\mu\text{m}$, both simulated and as data obtained directly from the oscilloscope screen.

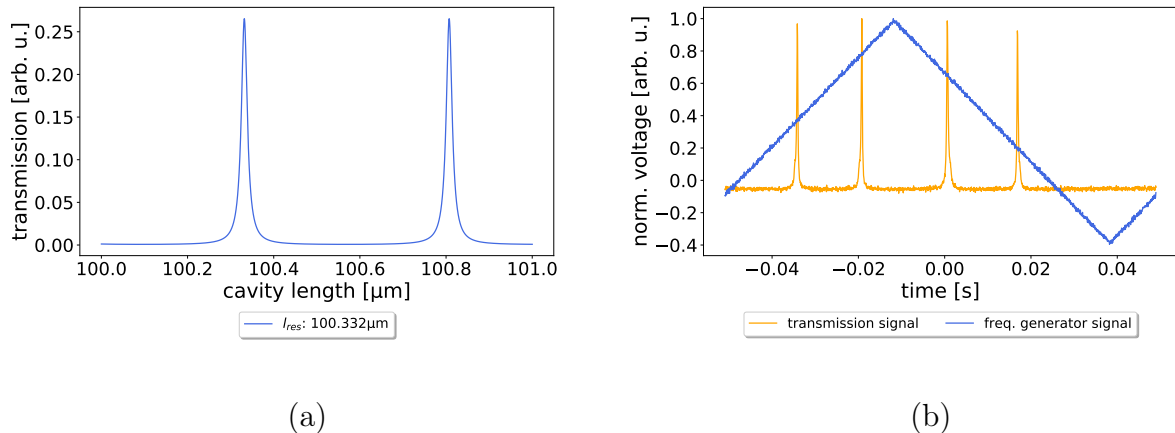


Figure 44: (a) shows a simulated length scan of range $1\mu m$ for a symmetric lossless double Fano cavity of length $\sim 100\mu m$. The labeled resonant length l_{res} in the figure indicates the first length found that fulfills the brightness condition. (b) is a plot of raw data logged from the oscilloscope used to record cavity transmission data. The blue line shows the signal from a frequency generator which is applied to the piezo ring, i.e. it correlates to the piezo expansion and thus a change in the cavity length. The orange line represents normalized cavity transmission intensity as a function of time, i.e. the cavity length. Note that the triangular signal is necessary in order to uniformly expand and compress the piezo ring. This ensures that the FSR stems from a linear expansion and that the piezo ring does not break from non-linear stress across the crystal structure.

When the fringes on the time-dependent length scan are visible while scanning with the piezo ring, they can be optimized by making small adjustments of the angular degrees of freedom of the top of the cavity, i.e. of G_2 . The parallelism of the cavity is an important parameter for a cavity of high finesse, and while normal incidence have here been achieved for G_1 and G_2 individually, both Fano mirrors have since been removed and re-inserted into the setup, which introduces uncertainty regarding the fine-tuning of the alignment. Especially the top of the cavity, which is fastened on nothing more than an optical post from Thorlabs and thus have only approximate reproducibility of the angular alignment (this is seen in figure 35), is prone to uncertainties hereof after re-insertion. For this reason the parallelism is optimized using the fringes on the oscilloscope. The parallelism is outlined in greater detail in section 3.3.6.

When the fringes of the time-dependent signal have been optimized fully, the frequency generator is then turned off and the fringes disappear. The piezo driver

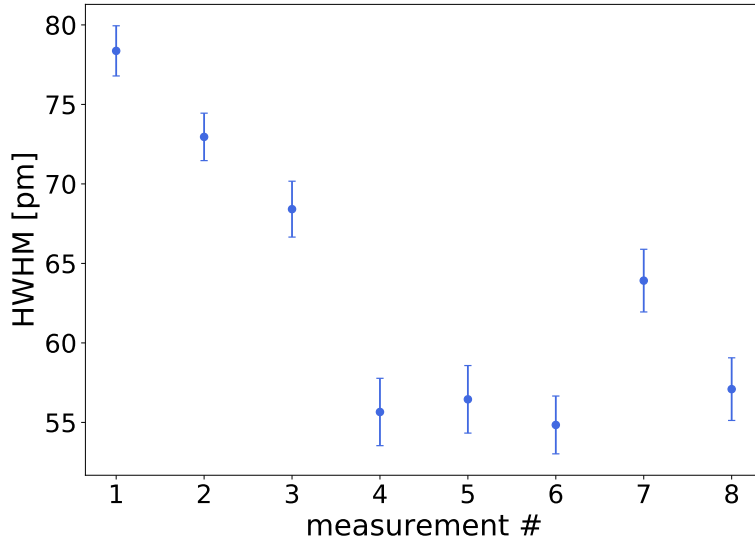


Figure 45: Linewidth as a function of "time" of an approximately $452\mu m$ double Fano cavity. It is clear that the linewidth generally decreases with time as a baseline for the HWHM is reached. This is assumed to be due to the drift of the piezo ring, while it must be noted that this is not possible to conclude indefinitely from the presented data. "Time" is to be understood as the chronological order in time, as the measurements are presented in the order in which they were recorded in the lab.

is now used to manually apply a constant voltage to expand the piezo gradually until the signal through the Fano cavity is maximized. This corresponds to the point where the cavity length and thus the cavity mode is resonant with the guided-modes of G_1 and G_2 .

The piezo ring, while capable of tuning the cavity length on a very small scale, tends to drift with time. This drift is apparent when the constant voltage is applied as the signal tends to decrease with time after optimization of the transmission. The piezo drift is more pronounced when the measurement session is first started and the time it takes for the piezo to lengthen or shorten becomes longer when a constant voltage have been applied to the piezo for some time. For this reason the measurements of the Fano resonance transmission profiles tend to be broader at first, and then gradually converge to the optimal value as more measurements are conducted. Note however, that this varies greatly depending on the adjustments made throughout a measurement session. Figure 45 shows linewidths of the resonance transmission profile, of an arbitrarily chosen double Fano cavity, as a function of "time". "Time" is referring to the fact that the

measurements are plotted in chronological order with respect to the time of measurement.

3.3.3 Determining the cavity length

Now the double Fano cavity is aligned and the cavity-, laser- and guided-modes all coincide to a high enough degree to sustain a Fano resonance mode. However, before doing the actual optical characterization, the cavity length must first be determined. In the end we want to plot the linewidth of the double Fano resonance spectra as a function of the cavity length, and in order to do so we must measure both.

Here we remember that the Fano cavity, when off-resonance, acts simply as a Fabry-Perot interferometer, which means that the off-resonance spectrum abides by the relations outlined in section 2.1. More specifically we know that the FSR relates to the cavity length according to eq. (??), which can be re-interpreted, and re-written, as

$$l = \frac{\lambda_0^2}{2FSR}, \quad (57)$$

where λ_0 is the cavity resonance wavelength.

So, to have a qualitative measure of the cavity length while doing measurements in the lab, off-resonance spectra are recorded and by estimating the FSR from the live data the approximate cavity length is determined.

In order to obtain precise information on the length of a given cavity, we conduct more precise data analysis on the recorded off-resonance spectra. Figure 46 shows two examples of off-resonance spectra for two cavities of different length. The lengths are found as a fitting parameters from a least squares fit of the recorded data to the Fabry-Perot transmission function found in eq. (4).

3.3.4 Recording normalized spectra

The normalized spectra are now recorded in largely the same way as for the individual Fano mirrors in section 3.2, a series of measurements is necessary in order to obtain meaningful spectra that are normalized with respect to the light incident on the cavity. The needed measurements are the following:

1. The transmission through the Fano cavity recorded in photo detector P_T where the corresponding values for the measured amplitudes are denoted

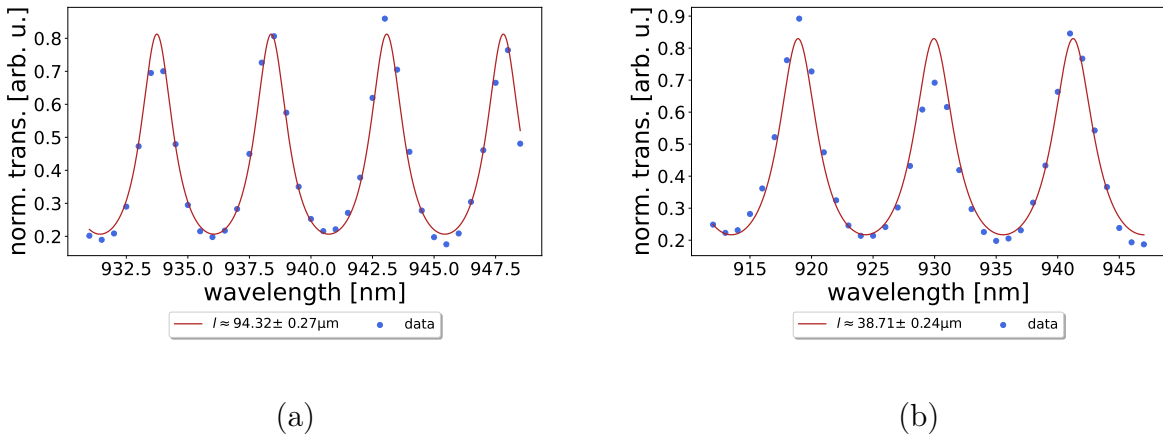


Figure 46: Off-resonance spectra of double Fano cavities of lengths $94.32 \pm 0.27\mu m$ (a) and $38.71 \pm 0.24\mu m$ (b). The lengths are found as fitting parameters from a least square fit of the recorded data to the Fabry-Perot transmission function in eq. (4), and the errors presented are found as the square root of the diagonal of the covarians matrix corresponding to the fit [17]. Note that the FSR increases when the cavity length decreases, as predicted in eq. (??).

T .

2. The light recorded in photo detector P_I during the transmission measurement. The corresponding values for the measured amplitudes are denoted T_I .
3. The light recorded in photo detector P_T when no cavity is present in the setup. This is denoted P'_T . The corresponding values for the measured amplitudes are denoted T' .
4. The light recorded in detector P_I during the transmission measurement with no cavity present. This is similarly denoted P'_I . The corresponding values for the measured amplitudes are denoted T'_I .

The normalized transmission values are then given as

$$T_{norm} = \frac{T/T_I}{T'/T'_I}, \quad (58)$$

which is the exact formula used for the Fano mirror characterization, except for the subtraction of the background which has here been assumed negligible. Examples of the four measurements are seen in figure 47, and the normalized spectrum is correspondingly seen in figure 48.

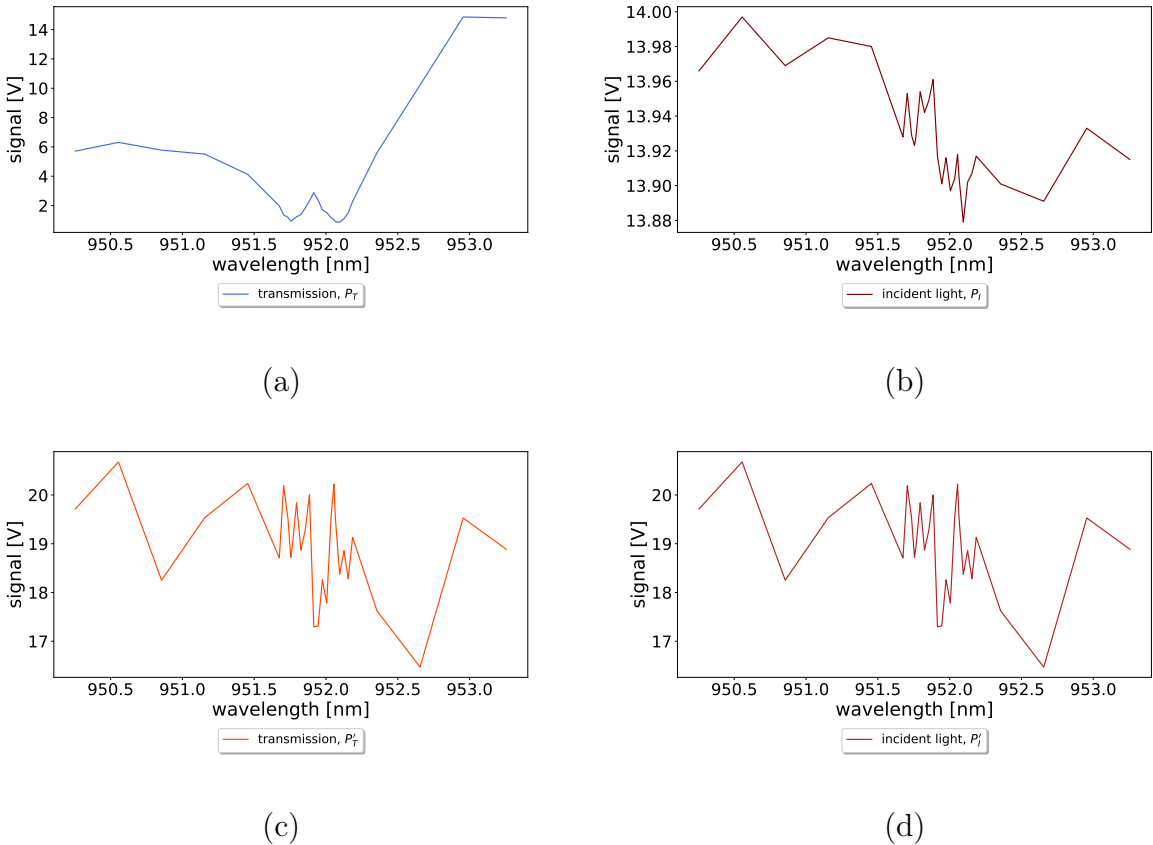


Figure 47: Examples of the four measurements used to produce the normalized transmission spectrum of the double Fano cavity (the same naturally applies for the single Fano cavity transmission). (a) shows the transmission through the double Fano cavity, (b) shows the incident light on the cavity, (c) shows the "transmission" when no cavity is present and (d) shows the light recorded by the incidence detector with no cavity present. All data is recorded for the same cavity of length $l = 21.390 \pm 0.119\mu m$. Note that the spectra in (c) and (d) seem identical. This is to be expected as they are simply measurements of a beam in each arm of a 50/50 beam splitter.

3.3.5 Centering of the top grating

When aligning the top part of the cavity setup seen in figure 34, it is crucial to ensure that the beam passes through the center of the rotational mount. Even the slightest deviation from the center can cause the alignment to be tedious at best, but likely practically impossible. The reason for this is the need for invariance in the xy-plane when aligning the Fano mirror for the fixed polarization of the laser. If the deviation from the center is too large, it might

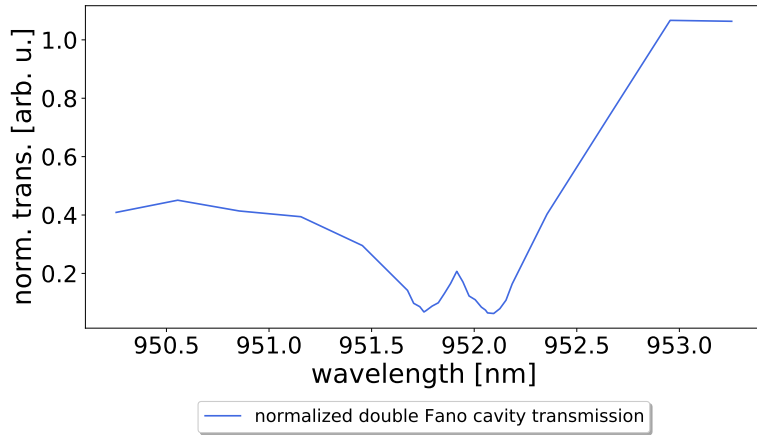


Figure 48: The normalized transmission spectrum for a double Fano cavity of length $l = 21.390 \pm 0.119\mu m$ calculated from the data depicted in figures 47a-d using eq. (58).

be impossible to tell whether the change in the transmitted intensity stems from moving further or closer to the optimal polarization, or if the Fano mirror is simply moving in and out of the beam. For this alignment a pinhole was designed to fit with high precision into the rotational mount in which it was fastened with a one inch (*SM1*) retainer ring from Thorlabs. A simple sketch of the pinhole is seen in figure 49a.

By moving the xy-stages in the cavity setup, it proved possible to achieve the centering of the rotational mount by moving the setup, with the pinhole inserted, until the transmission signal was maximized. Another test of the alignment was here to rotate the mount and thus pinhole and ensure that the signal intensity was as close to rotationally invariant as possible. Figure 50 shows an arbitrary gaussian distribution resembling the transverse distribution of a laser beam in the TEM00 mode and two shaded regions imitating the position of the pinhole. The red shaded region shows an *unaligned* pinhole position while the green one is perfectly *aligned* in the center of the beam. It is shown on the figure that the red area covers an intensity corresponding to 15.8% of the maximum intensity, while this value for the aligned green region is approximately double at 30.53%.

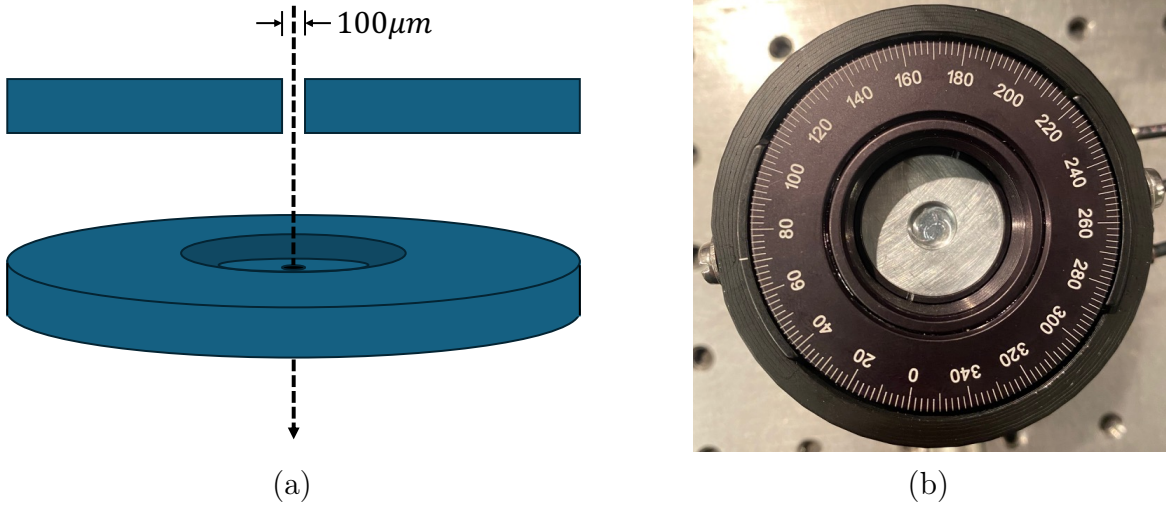


Figure 49: In (a) is a sketch of the pinhole used for centering the rotational- and kinetic mirror mounts in the incident beam. The side view of the pinhole is included to mark the pinhole diameter clearly while the angled view provides a visual representation of the actual component. (b) shows a picture of the rotational mount, seen from the top, with the pinhole inserted.

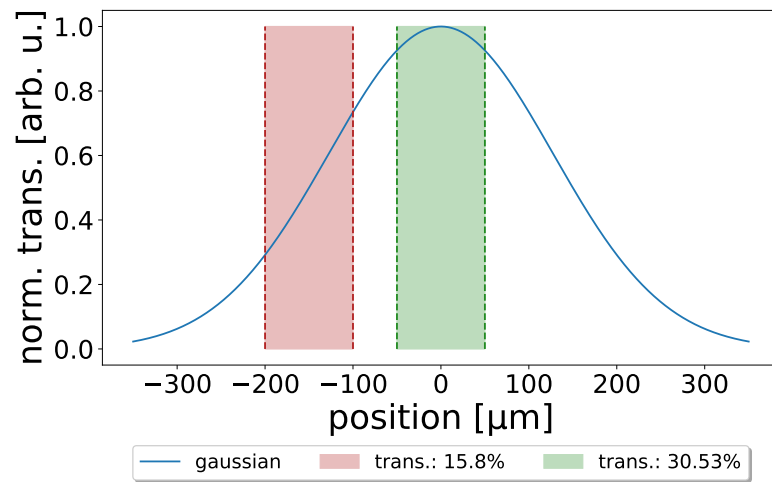


Figure 50: A gaussian distribution corresponding to the transverse distribution of a laser in the TEM00 mode. The red shaded region indicates a position for the pinhole with a transmission of 15.8% while the green one indicates a position with a transmission of 30.53%. The spacial dependence of the transmission through the pinhole is thus clearly displayed.

3.3.6 Estimating parallelism

A key difference between the single and double Fano cavity transmission spectra, is the off-resonance behavior. While the maximum transmission intensity for the single Fano will generally be lower than the Fano resonance peak, the opposite tends to be the case for the double Fano cavity. The direct reflectivities and transmissions r_d and t_d are similar, if not identical, for the two Fano mirrors, which means that the off-resonance Fabry-Perot-like transmission reaches a maximum of close to unity. The initial alignment of the cavity can thus be done by maximizing the off-resonance fringes. Due to the much broader peaks in this spectral regime, the fringes will be much less sensitive than the resonance peak. For this reason additional optimization is likely necessary.

Nair et al. [18] has proposed an analytical formula to estimate the wedge angle by considering the maximum transmission T_{MAX} of these Fabry-Perot fringes. T_{MAX} is given as

$$T_{MAX} \approx 1 - \left(\frac{F\pi w_0}{\lambda} \right)^2 \varepsilon^2, \quad (59)$$

for a cavity of identical resonators, and as this is not necessarily the case for an arbitrary double Fano cavity we make the substitution $1 \rightarrow T_{MAX}^{optimal}$ to include the highest possible transmission given a set of compatible Fano mirrors. The expression now simply reads

$$T_{MAX} \approx T_{MAX}^{optimal} - \left(\frac{F\pi w_0}{\lambda} \right)^2 \varepsilon^2, \quad (60)$$

where $T_{MAX}^{optimal}$ is the maximum transmission for a wedge angle of 0, w_0 is the beam waist, λ is the wavelength, ε is the wedge angle in radians and F is the coefficient of finesse [2] given as

$$F = \frac{4R}{(1-R)^2}. \quad (61)$$

Rearranging this, for the wedge angle ε we get

$$\varepsilon \approx \sqrt{\left(T_{MAX}^{optimal} - T_{MAX} \right)} \left(\frac{\lambda}{F\pi w_0} \right). \quad (62)$$

An example of a normalized off-resonance transmission spectrum of a double Fano cavity is shown in figure 51. The blue line indicates a least squares fit of

the data points to the Fabry-Perot transmission function seen in eq. (4), while the red line indicates the optimal transmission for the same Fano mirrors as was used for the measurement. The maximum transmission recorded and the optimal value was found as

$$T_{MAX} = 83.3\% \quad \text{and} \quad T_{MAX}^{optimal} = 97.1\%, \quad (63)$$

which yields for the wedge angle

$$\varepsilon \approx 0.24 \text{ mrad} = 0.014^\circ, \quad (64)$$

assuming a beam waist of $w_0 = 160 \mu\text{m}$ and direct reflectivities and transmissions $r_d = 57\%$, $r'_d = 57.5\%$ and $t_d = t'_d = 81.4\%$.

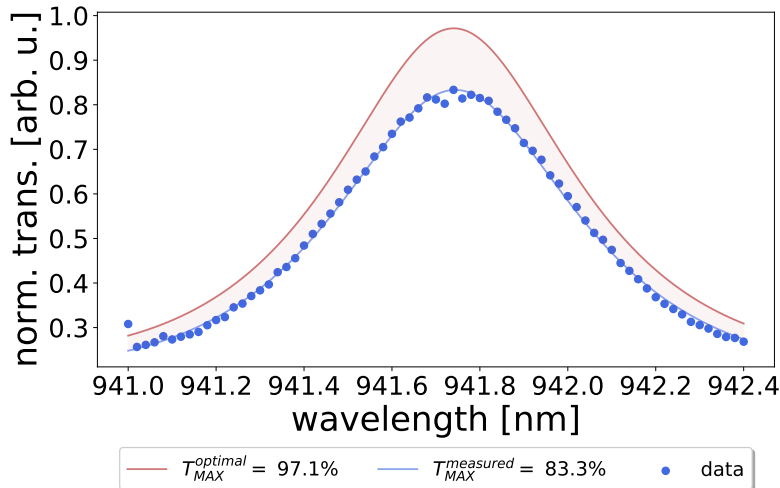


Figure 51: Example of a normalized off-resonance transmission peak of a double Fano cavity of direct reflectivities $r_d = 57\%$ and $r'_d = 57.5\%$ and direct transmissions $t_d = t'_d = 81.4\%$. The blue line is a least squares fit of the data to the Fabry-Perot transmission function while the red line is the optimal value of the same function. The red shaded area indicate the differnce between the two.

It is thus clear that while the sensitivity is of the off-resonance Fabry-Perot fringes is lower than that of the Fano resonance peak, they still provide a significant measure of the parallelism and is thus useful for initial cavity alignment.

4 Simulations

4.1 The single Fano cavity

4.2 The double Fano cavity

Figures:

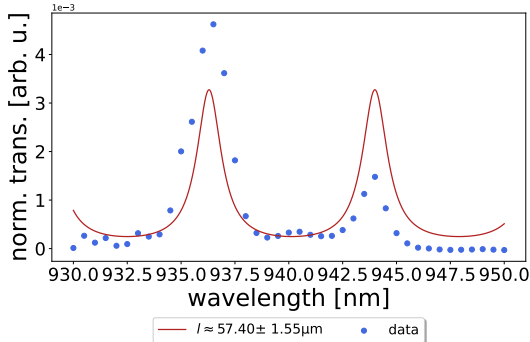
- Simulated spectra of M3 and M5.
- Simulated length scans of M3 and M5.
- M3/M5 cavity trans. spectra (on resonance + full range)
 - for lengths: $l_{M3} \rightarrow l_{M5}$
 - for length: $l = 1/2 \cdot (l_{M3} + l_{M5})$
- Optimal result comparison with single fano/broadband cavities of similar losses.
- Optimal result comparison with the ideal case from prev. section.
- Simulated linewidth as a function of cavity length (include the same for broadband and single fano cavities).

5 Experimental results

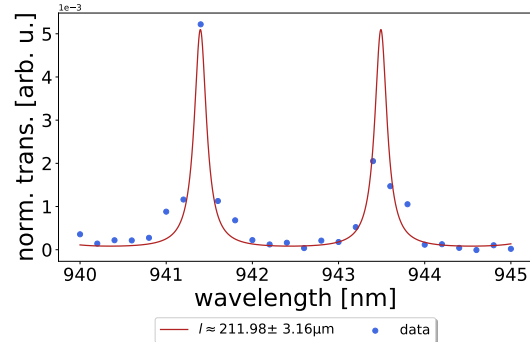
5.1 The single Fano cavity

Figures:

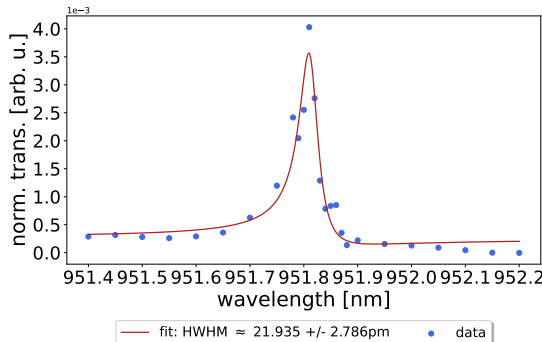
- Single fano cavity transmission as a function of wavelength.
- Short scan of the single fano cavity transmission, with found linewidth.
- Long scan Fabry-Perot fringes for determining FSR -> cavity length.
- linewidth as a function of cavity length (compare with broadband cavity).



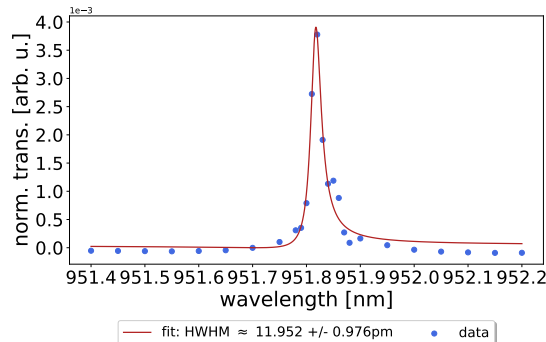
(a)



(b)



(a)



(b)

5.2 The double Fano cavity

5.2.1 Realizing the double fano model

Figures:

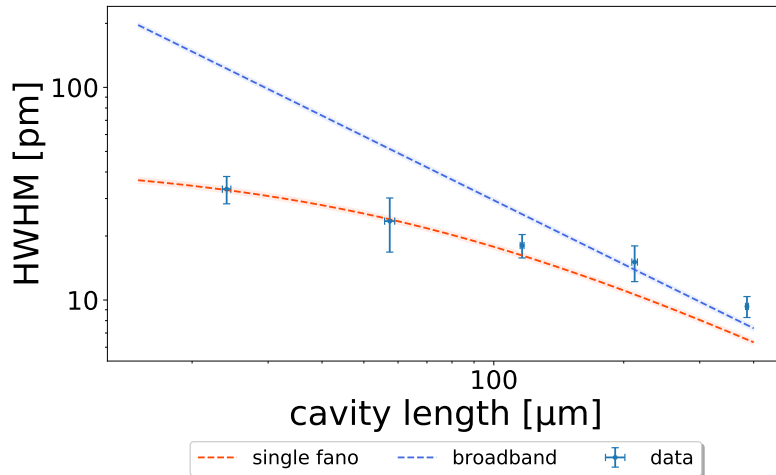


Figure 54

- Fit of the double fano model (long + short cavity)

5.2.2 Double fano off-resonance Fabry-Perot cavity

Figures:

- Off-resonance double fano transmission as a function of wavelength (show that the off resonance transmission goes close to 100 percent for a well-aligned cavity).

5.2.3 The double fano linewidth

Figures:

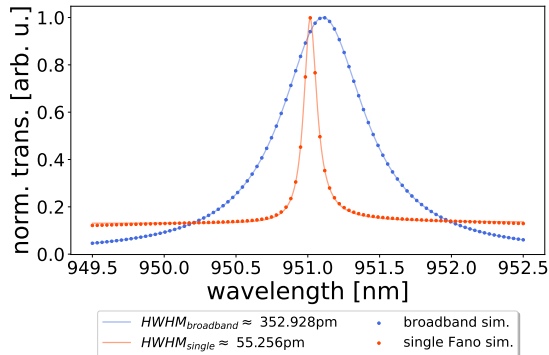
- "Semi-short" scan data, fit to the double fano transmission model.
- Short scan data, fit to the Fano function (for measuring linewidth).
- Linewidth as a function of cavity length (compare double fano, single fano and broadband cavitites).

6 Discussion

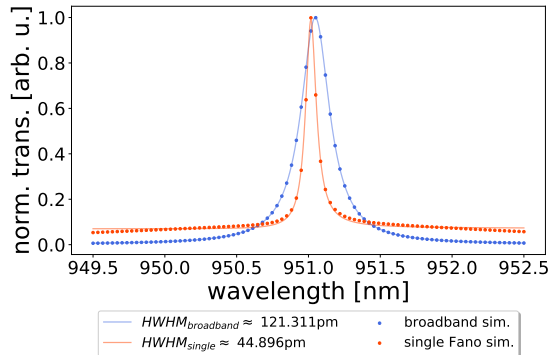
- 6.1 Optimal configuration for double fano cavity - spacial limitation for the cavity length
- 6.2 Spacial drift of the piezo ring
- 6.3 Noise reduction - coupled/uncoupled mechanical/acoustic vibration (the plexi-glass box)
- 6.4 Broadening sources (especially for long cavities)
- 6.5 Improvements to the setup

7 Appendix

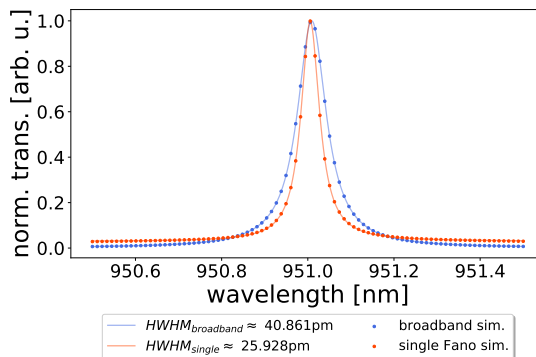
7.1 Simulated broadband and single Fano cavity resonance transmission spectra



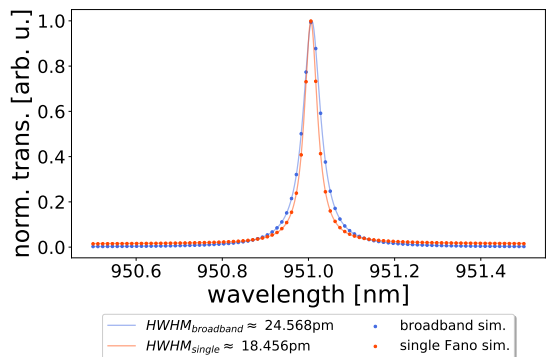
(a)



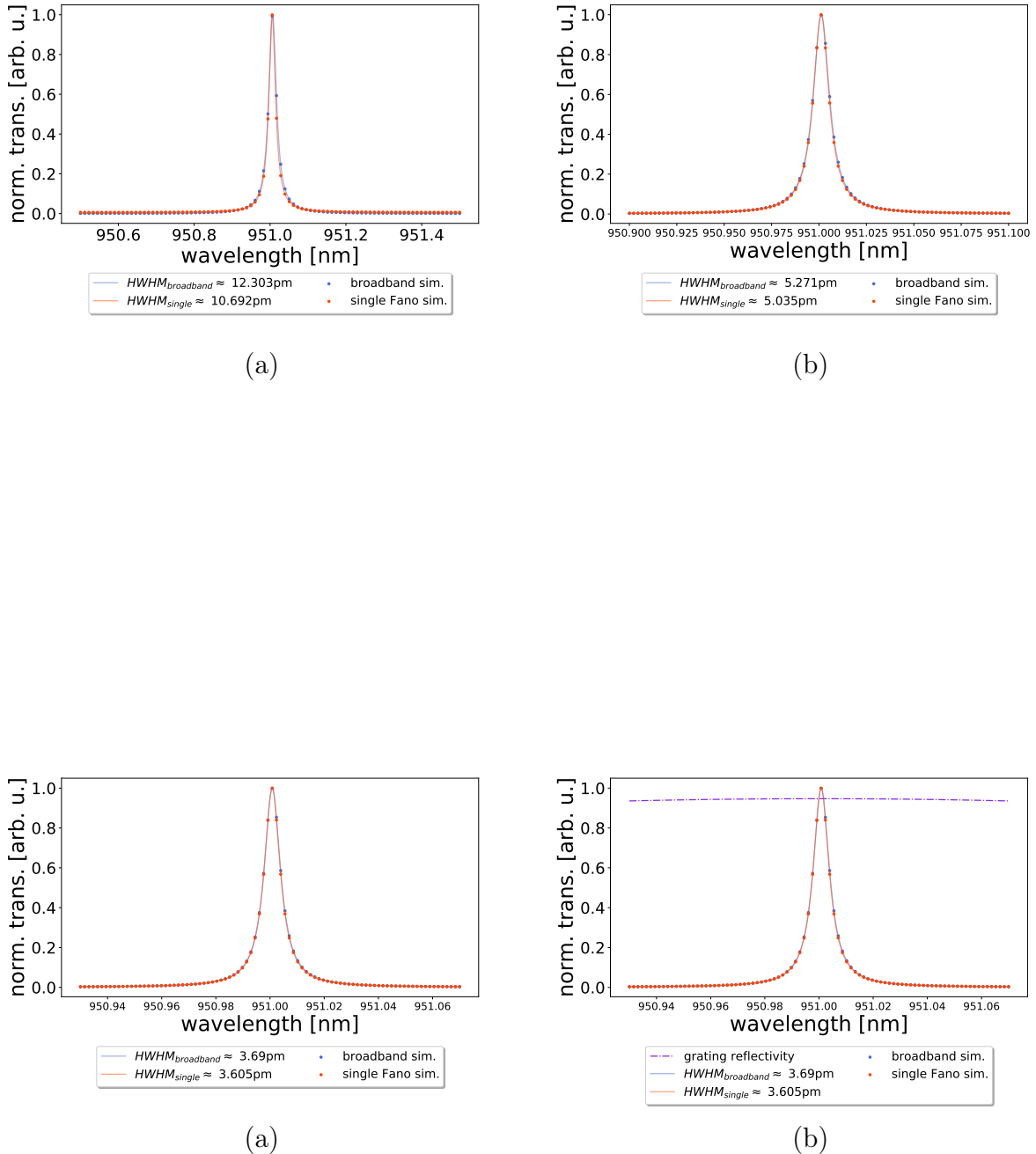
(b)



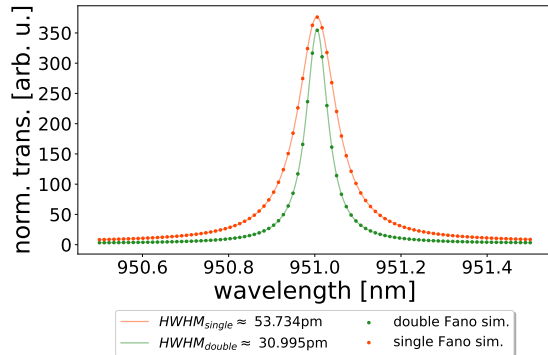
(a)



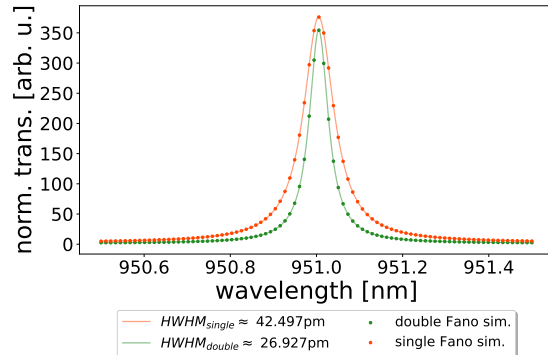
(b)



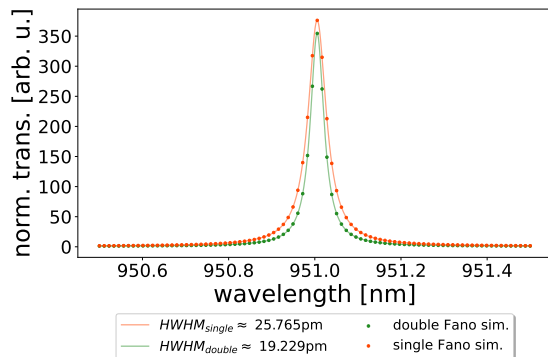
7.2 Simulated single and double Fano cavity resonance intracavity spectra



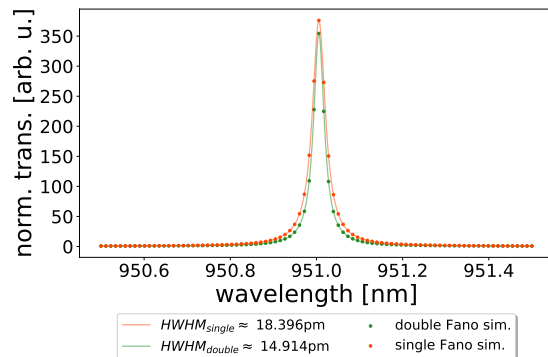
(a)



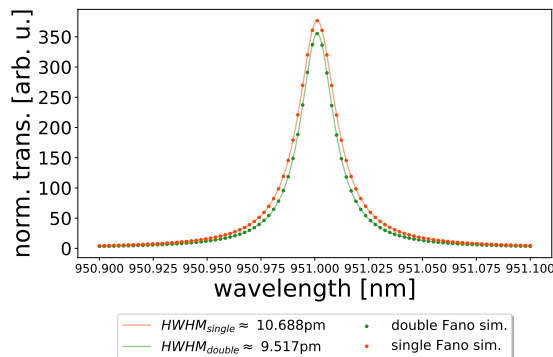
(b)



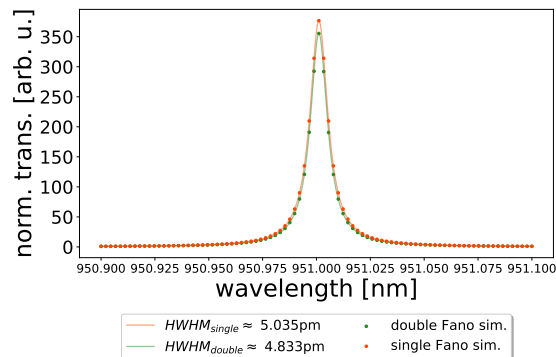
(a)



(b)



(a)



(b)

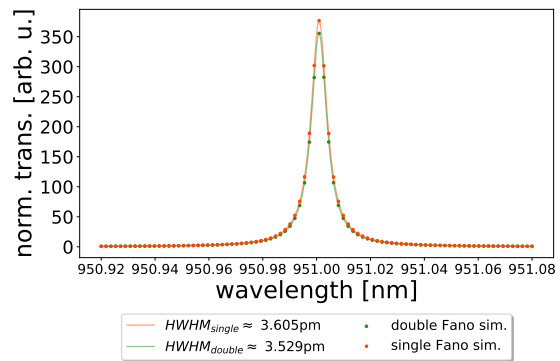


Figure 62

Things to add to appendix:

- The derivation of equation 33
- The derivation of equation 34
- Same derivations for the double fano cavity.

8 References

- [1] Marc Eichhorn. *Laser Physics - From Principles to Practical Work in the Lab.* Springer International Publishing Switzerland, 2014.
- [2] Frank L. Pedrotti, Leno M. Pedrotti, and Leno S. Pedrotti. *Introduction to Optics, 3rd edition.* Cambridge University Press, 2018.
- [3] Shanhui Fan and J. D. Joannopoulos. “Analysis of guided resonances in photonic crystal slabs”. In: *Physical Review B* 65 (2002).
- [4] U. Fano. “Effects of Configuration Interaction on Intensities and Phase Shifts*”. In: *Physical Review* 124.6 (1961).
- [5] Dmitry A. Bykov and Leonid L. Doskolovich. “Spatiotemporal coupled-mode theory of guided-mode resonant gratings”. In: *Optical Society of America* 14.3 (2015).
- [6] A. A. Darki et al. “Profilometry and stress analysis of suspended nanosstructured thin films”. In: *Journal of Applied Physics* (2021).
- [7] A. Parthenopoulos et al. “Optical spatial differentiation with suspended subwavelength gratings”. In: *Optics Express* 29.5 (2021).
- [8] E. Popov, L. Mashev, and D. Maystre. “Theoretical Study of the Anomalies of Coated Dielectric Gratings”. In: *Optica Acta: International Journal of Optics* 33.5 (1986).
- [9] URL: <https://pages.nist.gov/ScatterMIST/docs/index.htm>.
- [10] C. Toft-Vandborg et al. “Collimation and finite-size effects in suspended resonant guided-mode gratings”. In: *Journal of the Optical Society of America* 38.11 (2021).
- [11] Ali Akbar Darki. “Nanostructured trampolines for photonics and sensing”. PhD thesis. Department of Physics and Astronomy - Aarhus University, 2022.
- [12] T. Mitra et al. “Narrow-linewidth Fano microcavities with resonant subwavelength grating mirror”. In: *Optics Express* 32.9 (2024).
- [13] A. Naesby and A. Dantan. “Microcavities with suspended subwavelength structured mirrors”. In: *Optics Express* 26.23 (2018).
- [14] URL: <https://www.edmundoptics.com/knowledge-center/application-notes/optics/understanding-waveplates/>.

- [15] S. Yu. Sadov and K. A. McGreer. “Polarization dependence of diffraction gratings that have total internal reflection facets”. In: *J. Opt. Soc. Am. A* 17.9 (2000).
- [16] M. Forster et al. “213 nm and 532 nm solid state laser treatment of biogenetical fibrous materials”. In: (2010).
- [17] Ifan G. Hughes and Thomas P.A. Hase. *Measurements and their Uncertainties - A Practical Guide to Modern Error Analysis*. Oxford University Press, 2010.
- [18] B. Nair, A. Naesby, and A. Dantan. “Optomechanical characterization of silicon nitride membrane arrays”. In: *Optics Letter* 42.7 (2017).